Radiative, two-temperature simulations of low luminosity black hole accretion flows in general relativity

Aleksander Sądowski[1,2]⋆, Maciek Wielgus[3]†, Ramesh Narayan[4], David Abarca[3], Jonathan C. McKinney[5] and Andrew Chael[4]

[1] *MIT Kavli Institute for Astrophysics and Space Research, 77 Massachusetts Ave, Cambridge, MA 02139, USA*
[2] *Einstein Fellow*
[3] *Nicolaus Copernicus Astronomical Center, Bartycka 18, Warsaw 00-716, Poland*
[4] *Harvard-Smithsonian Center for Astrophysics, 60 Garden St., Cambridge, MA 02134, USA*
[5] *Department of Physics and Joint Space-Science Institute, University of Maryland, College Park, MD 20742*

arXiv:1605.03184v2 [astro-ph.HE] 3 Dec 2016

6 December 2016

ABSTRACT

We present a numerical method which evolves a two-temperature, magnetized, radiative, accretion flow around a black hole, within the framework of general relativistic radiation magnetohydrodynamics. As implemented in the code KORAL, the gas consists of two subcomponents – ions and electrons – which share the same dynamics but experience independent, relativistically consistent, thermodynamical evolution. The electrons and ions are heated independently according to a prescription from the literature for magnetohydrodynamical turbulent dissipation. Energy exchange between the particle species via Coulomb collisions is included. In addition, electrons gain and lose energy and momentum by absorbing and emitting synchrotron and bremsstrahlung radiation, and through Compton scattering. All evolution equations are handled within a fully covariant framework in the relativistic fixed-metric spacetime of the black hole. Numerical results are presented for five models of low luminosity black hole accretion. In the case of a model with a mass accretion rate $\dot{M} \sim 4\times10^{-8}\dot{M}_{\rm Edd}$, we find that radiation has a negligible effect on either the dynamics or the thermodynamics of the accreting gas. In contrast, a model with a larger $\dot{M} \sim 4\times10^{-4}\dot{M}_{\rm Edd}$ behaves very differently. The accreting gas is much cooler and the flow is geometrically less thick, though it is not quite a thin accretion disk.

Key words: accretion, accretion discs – black hole physics – relativistic processes – methods: numerical

1 INTRODUCTION

Black holes are common. Almost every galaxy in the Universe is believed to harbor a supermassive black hole (SMBH) at its core, often visible as an active galactic nucleus, as well as millions of stellar mass black holes, a few of which accrete gas from companion stars in close binary systems and are visible as X-ray binaries. We now also know that binary black holes are numerous and that they merge while emitting gravitational waves (Abbott et al. 2016).

Because of the compactness of a black hole, the gas approaching its horizon liberates a large fraction of its binding energy. Some of this energy goes into electromagnetic radiation and makes black hole systems exceptionally bright - black holes in outbursts are often the brightest X-ray sources in their galaxies, and the central engines of Active Galactic Nuclei (AGN) can be seen from across the Universe. The energy and momentum extracted from an AGN strongly affect not only the inner cluster, but also the dynamics of the entire galaxy.

There are three well established regimes of black hole accretion. The lowest accretion rates result in the lowest densities of gas. Such accretion flows are optically thin and radiatively inefficient and correspond to the radio-mode of an AGN and the low-hard state and quiescent state of X-ray binaries (analytical models for such conditions were developed by, e.g., Narayan & Yi (1995) and Blandford & Begelman (1999), see Yuan & Narayan (2014), for a review). As the optical depth grows with increasing accretion rate, the gas cools more efficiently, and above a critical accretion rate a thin accretion disk is formed (Shakura & Sunyaev 1973). Finally, once the accretion rate and the corresponding disk luminosity approach the Eddington values (see next Section), photon trapping

⋆ E-mail: asadowsk@mit.edu (AS)
† E-mail: maciek.wielgus@gmail.com (MW)

© 0000 The Authors

and radiative driving of winds become important and modify the picture (e.g., Abramowicz et al. 1988).

Whenever gas is sufficiently dense, the electrons and ions equilibrate efficiently because of Coulomb coupling and their temperatures become equal. This fact greatly simplifies the physics involved - the plasma can be treated as a single temperature fluid with mean molecular weight reflecting its chemical composition.

Optically thin flows are more complicated. The Coulomb interaction is inefficient and the temperatures of electrons and ions can be very different. The actual distribution of energy between the species depends not only on the balance between radiative cooling (acting on electrons) and Coulomb coupling (bringing electrons and ion temperatures together), but also on how the electrons and ions are heated. The latter depends on microphysics which cannot be resolved in magnetohydrodynamical grid-based simulations such as the ones reported in this paper. Instead one has to make some strong assumptions or adopt sub-grid prescriptions, which are generally somewhat ad hoc since our understanding of the heating process is still limited (see Yuan & Narayan 2014, for a review).

So far, only accretion flows corresponding to the two limits, optically thin and thick, have been simulated consistently in the framework of multidimensional magnetohydrodynamics. Simulations of accretion at the lowest rates, $\dot{M} \lesssim 10^{-6}\dot{M}_{\rm Edd}$, for long have only been done using the single fluid approximation (e.g., Hawley 2000; Tchekhovskoy et al. 2010; Narayan et al. 2012; McKinney et al. 2012; Mościbrodzka et al. 2014).

In the case of an optically thin medium, the radiation field is dynamically unimportant and can be solved for in the postprocessing stage (e.g., Dexter et al. 2010; Shcherbakov et al. 2012; Chan et al. 2015a). Because only a single fluid (mixture of ions and electrons) is evolved in most MHD simulations, one has to choose, somewhat arbitrarily, what the electron temperature is, which ultimately determines the emitted radiation. Only recently has this method been improved. Ressler et al. (2015) introduced an independent second fluid, electrons, and they used a prescription for the heating of electrons and ions according to a physically motivated sub-grid model (Howes 2010). This approach leads to the ability to determine electron temperatures with fewer ad hoc prescriptions.

In the case of an optically thick gas, one does not need to distinguish between electrons and ions - both have the same temperature because of efficient Coulomb coupling. However, in such cases, radiation is dynamically important and has to be solved in parallel with the evolution of the gas and the magnetic field. Recent developments in global simulations of accretion flows of this kind (corresponding to accretion rates $\dot{M} \gtrsim 10^{-3}\dot{M}_{\rm Edd}$) include the pioneering works of Ohsuga et al. (2009) and Ohsuga & Mineshige (2011), as well as Sądowski et al. (2013, 2014); McKinney et al. (2014); Fragile et al. (2014), who applied general relativistic M1 closure, Jiang et al. (2014) who directly solved the radiation transfer equation in a Newtonian potential, and Ryan et al. (2015) who solved the equations of general relativistic radiation MHD using a direct Monte Carlo solution of the frequency-dependent radiative transport equation.

None of these methods are appropriate in the regime in between, $10^{-6}\dot{M}_{\rm Edd} \lesssim \dot{M} \lesssim 10^{-3}\dot{M}_{\rm Edd}$. At such accretion rates, radiative cooling starts to affect the gas temperature, but the cooling is not as efficient as in the optically thick case. Coulomb coupling brings the electron and ion temperatures towards each other, but does not yet equalize them.

The intermediate regime of accretion rates is relevant both for supermassive and stellar mass BHs. Many bright AGN are in this state, with M87 (e.g., Biretta et al. 1991) being a prominent example. X-ray binaries spend significant fraction of their lifetime at such low accretion rates. During the hard-to-soft transition, the accretion rate increases and the system often enters the high-soft, optically thick, state. Understanding the nature of this transition, and the physical processes behind the related phenomena, e.g., iron line reflection and quasi periodic oscillations, will not be possible without detailed numerical modelling of accretion flows in the intermediate regime.

In this paper we introduce a hybrid algorithm which evolves the gas and radiation fields together in parallel, and accounts for their exchange of energy and momentum. At the same time, the algorithm evolves electrons and ions as two separate fluids affected by radiative cooling, Coulomb coupling, and viscous heating. This algorithm has been implemented in a general relativistic radiative magnetohydrodynamic (GRRMHD) code `KORAL`. We also present and adopt sophisticated synchrotron and bremsstrahlung grey opacities. Such a combination allows us, for the first time, to consistently simulate accretion flows in the intermediate regime.

The paper is organized as follows. In Section 2 we give all the essential equations describing conservation of mass, energy and momentum, electron and ion entropy evolution, viscous heating, Coulomb coupling, and the radiative coupling term. In particular, in Section 2.4 we give an expanded form of the opacities. In Section 3 we describe in detail the numerical algorithm, which we test in Section 4. In Section 5 we present and discuss simulations of low luminosity accretion flows. Finally, in Section 6 we discuss various caveats, and we conclude in Section 7.

1.1 Units and formalism

In this work we adopt the following definition for the Eddington mass accretion rate,

$$\dot{M}_{\rm Edd} = \frac{L_{\rm Edd}}{\eta c^2}, \tag{1}$$

where $L_{\rm Edd} = 4\pi GMm_{\rm p}c/\sigma_{\rm T} = 1.25\times10^{38}M/M_\odot\,{\rm erg/s}$ is the Eddington luminosity for a BH of mass M, and η is the radiative efficiency of a thin disk around a black hole with a given spin $a_* \equiv a/M$. For a zero BH spin, the case considered in this paper, $\eta \approx 0.057$ and $\dot{M}_{\rm Edd} = 2.48\times10^{18}M/M_\odot\,{\rm g/s}$. Hereafter, we use the gravitational radius $r_{\rm g} = GM/c^2$ as the unit of length, and $t_{\rm g} = r_{\rm g}/c$ as the unit of time.

2 PHYSICS

2.1 Standard set of equations

The conservation laws for gas density, its energy and momentum, radiation energy and momentum, and photon number can be written in covariant form,

$$(\rho u^\mu)_{;\mu} = 0, \tag{2}$$
$$(T^\mu_{\ \nu})_{;\mu} = G_\nu, \tag{3}$$
$$(R^\mu_{\ \nu})_{;\mu} = -G_\nu, \tag{4}$$
$$(nu^\mu)_{;\mu} = \dot{n}. \tag{5}$$

where ρ is the gas density in the comoving fluid frame, u^μ is the gas four-velocity, T^μ_ν is the MHD stress-energy tensor,

$$T^\mu_{\ \nu} = (\rho + u_{\rm int} + p + b^2)u^\mu u_\nu + (p + \frac{1}{2}b^2)\delta^\mu_{\ \nu} - b^\mu b_\nu, \tag{6}$$

with $u_{\rm int}$ and $p = (\gamma_{\rm int} - 1)u_{\rm int}$ representing the internal energy density and pressure of the gas in the comoving frame with adiabatic index, $\gamma_{\rm int}$ (as explained in Appendix A, we consider two different kinds of adiabatic index, $\gamma_{\rm int}$ and $\gamma_{\rm CV}$, one for the internal energy and one for the specific heat), R^{μ}_{ν} stands for the radiative stress-energy tensor and n for the photon number density, and b^{μ} is the magnetic field 4-vector which is evolved following the ideal-MHD induction equation (Gammie et al. 2003).

The radiative stress-energy tensor is obtained from the evolved radiative primitives, i.e., the radiative rest-frame energy density, $E_{\rm R}$, and its four-velocity, $u^{\mu}_{\rm R}$, following the M1 closure scheme modified by the addition of radiative viscosity (see Sądowski et al. 2013, 2015, for details).

The interaction between the gas and the radiation, i.e., the transfer of energy and momentum, is described by the radiation four-force density G_{ν}. The opposite signs of this quantity on the right hand sides of Eqs. 3 and 4 reflect the fact that the gas-radiation interaction is conservative, i.e., it transfers energy and momentum between gas and radiation. The detailed form of the four-force density is given and discussed in Section 2.3 and the relevant opacities are presented in Section 2.4 and Appendix A.

2.2 Evolution of ions and electrons

The set of equations (Eqs. 2-5) given above describes the evolution of the *total* gas energy density and momentum. The emission properties of the gas, however, depend mostly on the electrons. It is reasonable to assume that both electrons and ions move with the same bulk velocity, i.e., there is no need to consider their momenta independently. However, it is necessary to follow the energy content of the two species. In principle, it is enough to follow the energy of only one of the species because the total energy is evolved already in the standard set of equations. However, for the sake of symmetry and accuracy, and keeping in mind the very moderate cost of evolving another equation, we decided to follow the energy content in the electrons and ions independently.

We adopt an approach similar to the one taken by Ressler et al. (2015), i.e., we evolve ions and electrons adiabatically by conserving their entropy, and apply the non-adiabatic changes to their energy as source terms.

The entropy equations of the two species take the form,

$$T_{\rm e}(n_{\rm e}s_{\rm e}u^{\mu})_{;\mu} = \delta_{\rm e}q^{\rm v} + q^{\rm C} + G_t \tag{7}$$

$$T_{\rm i}(n_{\rm i}s_{\rm i}u^{\mu})_{;\mu} = (1-\delta_{\rm e})q^{\rm v} - q^{\rm C}, \tag{8}$$

where $T_{\rm e}$ and $T_{\rm i}$ are the temperatures of ions and electrons, respectively, $n_{\rm e}$ and $n_{\rm i}$ are the number densities, $s_{\rm e}$ and $s_{\rm i}$ are the entropies per particle (which are given in Section 2.2.1), $q^{\rm v}$ is the rate of dissipative heating, a fraction of which ($\delta_{\rm e}$) is applied to electrons, and the remaining part $(1-\delta_{\rm e})$ to ions (Section 2.2.2), $q^{\rm C}$ is the Coulomb coupling rate which describes energy exchange between electrons and ions (Section 2.2.3), and finally, G_t is the radiative heating/cooling rate which affects only electrons (Section 2.3). Setting the right hand side of Eqs. 7 and 8 to zero corresponds to adiabatic evolution of the species.

The electron and ion number densities are,

$$n_{\rm e,i} = \frac{\rho}{\mu_{\rm e,i} m_{\rm p}}, \tag{9}$$

where $m_{\rm p}$ is the proton mass and $\mu_{\rm e}$ and $\mu_{\rm i}$ are the mean molecular weights of electrons and ions, respectively, which, for zero metallicity, are given by,

$$\mu_{\rm e} = \frac{2}{1+X}, \tag{10}$$

$$\mu_{\rm i} = \frac{4}{4X+Y}, \tag{11}$$

where X and Y denote the relative mass abundances of hydrogen and helium. In the simulations presented in this paper we exclusively use $X = 1$, $Y = 0$.

2.2.1 *Entropy, Adiabatic Index and Temperature*

In this work we use the following approximate relativistic entropy formula derived in Appendix A,

$$s_{\rm e,i} = k \ln\left[\frac{\theta_{\rm e,i}^{3/2}\left(\theta_{\rm e,i} + \frac{2}{5}\right)^{3/2}}{\rho_{\rm e,i}}\right], \tag{12}$$

where $\theta_{\rm e,i} = kT_{\rm e,i}/m_{\rm e,i}c^2$ are the dimensionless temperatures of electrons and ions and $m_{\rm e,i}$ are the particle masses.

Inverting Equation (12), we can solve for the temperature θ as a function of the density and entropy per particle,

$$\theta_{\rm e,i} = \frac{1}{5}\left(\sqrt{1 + 25\left[\rho_{\rm e,i}\exp\left(\frac{s_{\rm e,i}}{k}\right)\right]^{2/3}} - 1\right). \tag{13}$$

2.2.2 *Viscous heating*

We measure the amount of the viscous heating affecting the gas, i.e., electrons and ions altogether, by comparing the non-adiabatic evolution according to the energy equation of the total gas (Eq. 3), with the adiabatic evolution of electrons and ions (Eqs. 7 & 8 with right hand sides set to zero). The former is expected to lead to a larger energy density than the latter, and the difference comes solely from viscous dissipation.

Therefore, the viscous heating rate in the comoving frame of the gas, $\widehat{q^{\rm v}}$, is given by,

$$\widehat{q^{\rm v}} = \frac{u_{\rm int} - u_{\rm e,adiab.} - u_{\rm i,adiab.}}{\Delta\tau}, \tag{14}$$

where $u_{\rm int}$ is the internal energy density of the total gas at the end of the explicit (convective) operator (see Section 3.2) obtained by evolving the time (energy) component of Eq. 3 over comoving frame time step $\Delta\tau$, and $u_{\rm e,adiab.}$ and $u_{\rm i,adiab.}$ correspond to the internal energies carried by electrons and ions, respectively, measured once again at the end of the explicit operator and obtained through the adiabatic evolution of their respective entropies.

The (adiabatic) energy densities of the electrons and ions are obtained from their entropy densities by first calculating their respective temperatures through Eq. 13. Knowing the temperatures, we may write down the electron and ion pressures,

$$p_{\rm e,i} = k\frac{\rho}{\mu_{\rm e,i} m_{\rm p}} T_{\rm e,i}, \tag{15}$$

and obtain the corresponding energy densities through,

$$u_{\rm (e,i),adiab.} = \frac{p_{\rm e,i}}{\gamma_{\rm int\,e,i} - 1}, \tag{16}$$

where $\gamma_{\rm int\,e,i}$ are the electron and ion adiabatic indices corresponding to their temperatures (Appendix A),

$$\gamma_{\rm int\,e,i} \approx \frac{10 + 20\theta_{\rm e,i}}{6 + 15\theta_{\rm e,i}}. \tag{17}$$

The total viscous heating rate, $q^{\rm v}$ (Eq. 14) is finally distributed

between electrons and ions. The fraction of heating going into electrons depends on the microscopic properties of a collisionless plasma. In this work we follow Ressler et al. (2015) and use the fitting formula of Howes (2010) for the fraction, δ_e, of the total heating that goes into electrons,

$$\delta_e = \frac{1}{1 + f(T_e, T_i, \beta)}, \tag{18}$$

$$f(T_e, T_i, \beta) = c_1 \frac{c_2^2 + \beta^{2-0.2\log_{10}(T_i/T_e)}}{c_3^2 + \beta^{2-0.2\log_{10}(T_i/T_e)}} \sqrt{\frac{m_i T_i}{m_e T_e}} \exp(-1/\beta)\,, \tag{19}$$

where β is the gas to magnetic pressure ratio, $c_1 = 0.92$, $c_2 = 1.6T_e/T_i$ and $c_3 = 18 + 5\log_{10}(T_i/T_e)$ if $T_i > T_e$, while we have $c_2 = 1.2T_e/T_i$ and $c_3 = 18$ for $T_i < T_e$.

2.2.3 Coulomb coupling

The ions and electrons exchange energy kinetically, through collisions. This effect is described by the comoving frame Coulomb coupling rate, which equals (Stepney & Guilbert 1983),

$$\widehat{q^C} = \frac{3}{2}\frac{m_e}{m_i}\overline{n}n_e \ln\Lambda \frac{ck\sigma_T(T_i - T_e)}{K_2(1/\theta_i)K_2(1/\theta_e)} \times \left[\frac{2(\theta_e+\theta_i)^2+1}{\theta_e+\theta_i}K_1(1/\theta_m) + 2K_0(1/\theta_m)\right]\left[\frac{\mathrm{erg}}{\mathrm{cm^3 s}}\right], \tag{20}$$

with $\theta_m = (1/\theta_e + 1/\theta_i)^{-1}$, $m_i = m_p(X + 4Y)$. K_i denotes the modified Bessel function of the i-th order and $\ln\Lambda \approx 20$ is the Coulomb logarithm. Number density $\overline{n}$ is defined as

$$\overline{n} = \sum_j (n_i)_j Z_j^2 = (X + Y)\rho/m_p = \rho/m_p, \tag{21}$$

where Z_j is the charge of the j-th species of ions, and the last equality holds for a pure mixture of hydrogen and helium. To avoid the computational problems related to evaluation of the Bessel functions for very large arguments, in the low temperature limit we continuously match them with the asymptotic formula

$$K_{0,1,2}(1/\theta) \approx \exp(-1/\theta)\sqrt{\frac{\pi\theta}{2}}. \tag{22}$$

2.3 Interaction of gas and radiation

2.3.1 Temperatures and the equation of state

Before we discuss in detail the interaction of gas and radiation we reiterate the various temperatures evolved in the code.

(i) T_g is the effective temperature of the gas (mixture of the electrons and ions). It is given through the ideal gas equation of state,

$$p_g = (\gamma_{gas} - 1)u_{int} = k\frac{\rho}{\mu m_p}T_g, \tag{23}$$

where p_g and u_{int} are the gas pressure and internal energy density, respectively, γ_{gas} is the effective adiabatic index of the electron and ion mixture (see below), and μ is the mean molecular weight,

$$\mu = \left(\frac{1}{\mu_i} + \frac{1}{\mu_e}\right)^{-1} = \frac{4}{6X + Y + 2}. \tag{24}$$

(ii) T_e and T_i are the ion and electron temperatures, respectively. They are obtained from the evolved entropy density through Eq. 13 and satisfy the respective equations of state,

$$p_{e,i} = (\gamma_{int\,e,i} - 1)u_{e,i} = k\frac{\rho}{\mu_{e,i} m_p}T_{e,i}. \tag{25}$$

The electron and ion pressures, p_e and p_i, satisfy,

$$p_g = p_e + p_i. \tag{26}$$

The temperatures must therefore satisfy,

$$T_g = \mu\left(\frac{T_i}{\mu_i} + \frac{T_e}{\mu_e}\right). \tag{27}$$

The effective adiabatic index for the electron and ion mixture is thus,

$$\gamma_{gas} = 1 + \frac{(\gamma_{int\,e} - 1)(\gamma_{int\,i} - 1)(T_i/T_e + \mu_i/\mu_e)}{(T_i/T_e)(\gamma_{int\,e} - 1) + (\mu_i/\mu_e)(\gamma_{int\,i} - 1)} \tag{28}$$

(iii) T_r is the characteristic temperature of radiation, calculated from the radiation energy density and photon number density. It roughly corresponds to the frequency at which the electromagnetic spectrum of radiation peaks in the fluid frame at a given time and location.

We make the simplifying assumption that the spectral energy density of radiation $\widehat{E}_\nu(\nu, T_r)$ corresponds to a diluted black body (grey body) spectrum, i.e.,

$$\widehat{E}_\nu(\nu, T_r) = \phi\widehat{B}_\nu(\nu, T_r) = \phi\frac{2h\nu^3}{c^2}\frac{1}{\exp(h\nu/kT_r) - 1}, \tag{29}$$

for a non-negative constant coefficient $\phi \leqslant 1$. KORAL tracks the total radiation energy density $\widehat{E}$, and photon density $\widehat{n}$ (see Sądowski & Narayan 2015), from which we obtain,

$$T_r = \frac{\widehat{E}}{2.7012k\widehat{n}} \quad , \quad \phi = \frac{\widehat{E}c}{4\sigma T_r^4}. \tag{30}$$

2.3.2 The coupling term

Gas and radiation exchange energy and momentum through absorption and scattering. This interaction is described by the source term - the radiative four-force, G_μ, which couples gas and radiation (Eqs. 3-4). In the comoving frame of the gas it takes the following form,

$$\widehat{G} = \rho\begin{bmatrix} \kappa_{P,a}\widehat{E} - 4\pi\kappa_{P,e}\widehat{B} + \widehat{G}_{t,\mathrm{Compt}} \\ (\kappa_R + \kappa_{es})\widehat{F^i} \end{bmatrix}. \tag{31}$$

Here $\widehat{B} = \sigma T_e^4/\pi$ is the black body radiance of the electrons, $\widehat{F^i}$ is the radiation flux in the fluid frame, and we sum the Rosseland and scattering opacities for simplicity (in principle, the Rosseland mean opacity should be a single integral over all opacities, including the scattering term). In this work we account for bremsstrahlung and synchrotron opacities, hence, each opacity coefficient $\kappa_{P,a}$ (energy mean absorption), $\kappa_{P,e}$ (energy mean emission) and $\kappa_{R,a}$ (Rosseland mean absorption) consists of bremsstrahlung and synchrotron components, i.e.,

$$\kappa_{P,e} = \kappa_{P,e}^{(ff)} + \kappa_{P,e}^{(sy)}, \tag{32}$$

$$\kappa_{P,a} = \kappa_{P,a}^{(ff)} + \kappa_{P,a}^{(sy)}, \tag{33}$$

$$\kappa_R = \kappa_R^{(ff)} + \kappa_R^{(sy)}. \tag{34}$$

These opacities are frequency-averaged, effective, gray opacities. There is no unique way of defining or computing these quantities since they depend on the precise frequency dependence of the radiation field. Mihalas & Mihalas (1984) recommend using the Planck mean opacity for the energy equation (time component of $\widehat{G}$) and the Rosseland mean opacity for the momentum equations (spatial components). This is the approach we take.

The electron scattering opacity, $\kappa_{\rm es}$, is responsible both for momentum and energy transfer. The latter is described through the Comptonization component, $\widehat{G^0}_{\rm Compt}$ (Sądowski & Narayan 2015),

$$\widehat{G^0}_{\rm Compt} = -\kappa_{\rm es}\rho\widehat{E}\left[\frac{4k(T_{\rm e}-T_{\rm r})}{m_{\rm e}c^2}\right]\times \left[1+3.683\left(\frac{kT_{\rm e}}{m_{\rm e}c^2}\right)+4\left(\frac{kT_{\rm e}}{m_{\rm e}c^2}\right)^2\right]\left[1+\left(\frac{kT_{\rm e}}{m_{\rm e}c^2}\right)\right]^{-1}. \quad (35)$$

2.4 Opacities

In our opacity model we make several improvements over the previous global GRRMHD simulations such as those reported in Dibi et al. (2012); Fragile et al. (2014); McKinney et al. (2014); Sądowski & Narayan (2015). As indicated by Eq. 31, we distinguish between the energy mean (Planck mean) opacities used for the energy term $\widehat{G^0}$ and the Rosseland mean opacities that are used in the momentum equations. However, as discussed in Mihalas & Mihalas (1984), there is no single gray opacity that is accurate in every opacity regime. We use the energy mean opacity for the energy equation to capture proper energy balance and the Rosseland mean opacity for the momentum equation in order to capture the proper flux in the diffusion limit. We further distinguish between the emission opacities from the absorption opacities. The emission opacities are calculated for the local electron temperature $T_{\rm e}$, while absorption opacities account for the actual radiation temperature $T_{\rm r} \neq T_{\rm e}$. In this section we only give the relevant formulas. More detailed discussion and derivation is given in the Appendix B.

2.4.1 *Free-free*

We take the bremsstrahlung energy mean emission opacity to be,

$$\kappa^{\rm (ff)}_{\rm P,e}\rho = 6.2\times10^{-24}\overline{n}n_{\rm e}T_{\rm e}^{-7/2}\,\overline{g}\,R(T_{\rm e})\ [{\rm cm}^{-1}], \quad (36)$$

where we assume a Gaunt factor $\overline{g} = 1.2$ and employ a relativistic correction (Rybicki & Lightman 1979),

$$R(T_{\rm e}) = 1 + 4.4\times10^{-10}T_{\rm e}. \quad (37)$$

The absorption energy mean opacity is given in the following form

$$\kappa^{\rm (ff)}_{\rm P,a} = \kappa^{\rm (ff)}_{\rm P,e}\xi^{-3}\cdot 1.047\ln(1+1.6\xi), \quad (38)$$

where $\xi = T_{\rm r}/T_{\rm e}$. The absorption opacity, Eq. 38, reduces to the emission opacity, Eq. 36, for $\xi = 1$.
Another fit is provided for the Rosseland mean opacity,

$$\kappa^{\rm (ff)}_{\rm R} = \kappa^{\rm (ff)}_{\rm P,e}\xi^{-3}\cdot 14.12 f_{\rm R}(\xi), \quad (39)$$

where

$$f_{\rm R}(\xi) = \left(432.7 - 106.8\xi^{-3/5} + 43.17\xi^{-4/5} + 57.88\xi^{-1}\right)^{-1}. \quad (40)$$

When $T_{\rm r} = T_{\rm e}$, the Rosseland mean opacity is about 30 times less than the energy mean opacity. Corresponding opacities are derived in the Appendix B, Eqs. B12-B14.

2.4.2 *Synchrotron*

In Gaussian-cgs units the energy mean emission opacity is

$$\kappa^{\rm (sy)}_{\rm P,e}\rho = 1.59\times10^{-30}n_{\rm e}B^2T_{\rm e}^{-2}\ [{\rm cm}^{-1}], \quad (41)$$

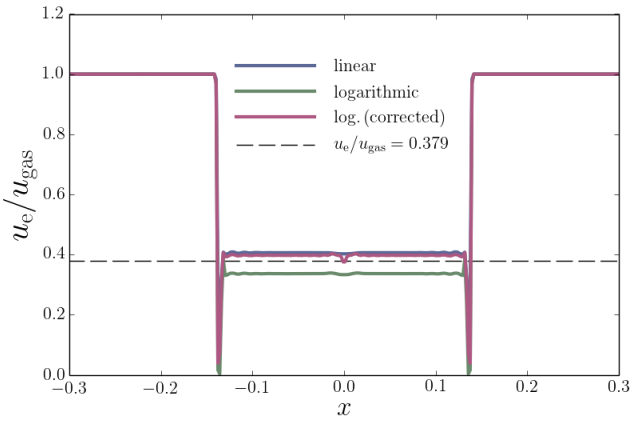

Figure 1. Profiles of the ratio of energy densities in electrons and gas for the 1D shock test described in Section 4.1. The corrected logarithm approach (eq. 52, see sec. 3.1) agrees best with the analytic solution $u_{\rm e}/u_{\rm gas} = 0.379$.

where $B^2 = 4\pi b^\mu b_\mu$. Numerical fits for the synchrotron opacities are given in terms of the dimensionless parameter ζ,

$$\zeta = \frac{4\pi m_{\rm e}^3c^5}{3ekh}\frac{T_{\rm r}}{BT_{\rm e}^2}. \quad (42)$$

The energy mean absorption opacity is numerically fitted as

$$\kappa^{\rm (sy)}_{\rm P,a} = \kappa^{\rm (sy)}_{\rm P,e}\xi^{-3}\left(1+5.444\zeta^{-2/3}+7.218\zeta^{-4/3}\right)^{-1}, \quad (43)$$

while the Rosseland mean opacity is given as

$$\kappa^{\rm (sy)}_{\rm R} = \kappa^{\rm (sy)}_{\rm P,e}\xi^{-3}\cdot 3.24\times10^{-2}\zeta^{1.31}\exp\left(-1.60\zeta^{0.463}\right). \quad (44)$$

We additionally fit the number mean opacity which is used in the photon density evolution equation,

$$\kappa^{\rm (sy)}_{\rm n} = \kappa^{\rm (sy)}_{\rm P,e}\xi^{-3}\cdot 0.868\zeta\left(1+0.589\zeta^{-1/3}+0.087\zeta^{-2/3}\right)^{-1}. \quad (45)$$

Corresponding opacities are derived in the Appendix B, Eqs. B27-B32.

2.4.3 *Scattering and Comptonization*

The Comptonization term $\widehat{G^0}_{\rm Comp}$ is given by Sądowski & Narayan (2015), and is a function of $T_{\rm e}$ and $T_{\rm r}$, scaled by the scattering opacity $\kappa_{\rm es}$. For $\kappa_{\rm es}$, we use the following energy and angle averaged Klein-Nishina formula (Buchler & Yueh 1976; Paczyński 1983), for consistency,

$$\kappa_{\rm es} = \kappa_{\rm T}\left[1+\left(\frac{T_{\rm r}}{4.5\times10^8K}\right)\right]^{0.86}\ [{\rm cm}^2{\rm g}^{-1}]. \quad (46)$$

In practice, for the radiation temperatures $T_{\rm r}$ that are found in the presented simulations, the Klein-Nishina correction to the Thomson scattering, $\kappa_{\rm T} = 0.2(1+X)$, is unimportant.

2.5 Photon number density evolution

We follow the photon number density evolution scheme proposed by Sądowski & Narayan (2015), but using the above improved model of opacities. Hence, the number density of photons is evolved with the following equation

$$\widehat{\dot{n}} = \widehat{\dot{n}}_{\rm sy} + \widehat{\dot{n}}_{\rm ff} - \left(\kappa^{\rm (sy)}_{\rm n} + \kappa^{\rm (ff)}_{\rm n}\right)\rho\widehat{n}c, \quad (47)$$

representing the balance between emission and absorption of photons. The synchrotron emission of photons is evaluated as

$$\widehat{n}_{\rm sy} = 1.44\times10^5 B n_{\rm e}\ [{\rm cm^{-3}s^{-1}}], \tag{48}$$

and we use the following approximation for the bremsstrahlung process

$$\widehat{n}_{\rm ff} = \frac{\kappa^{\rm (ff)}_{\rm P,e}\rho 4\pi\widehat{B}}{2.7012kT_{\rm e}}. \tag{49}$$

The absorption term in Eq. 47 consists of a properly integrated and numerically fitted number mean opacity for the synchrotron process, Eq. 45, and bremsstrahlung number mean opacity, approximated with the absorption energy mean opacity given in Eq. 38, $\kappa^{\rm (ff)}_{\rm n} = \kappa^{\rm (ff)}_{\rm P,a}$. See Appendix B for details.

3 NUMERICAL METHODS

We use the GRRMHD code KORAL (Sądowski et al. 2013, 2014). In the original version of the code, gas, magnetic field, and radiation are evolved in a fixed spacetime described by an arbitrary metric. The magnetic field is evolved under the assumption of ideal MHD, i.e., assuming that the electric field vanishes in the gas comoving frame, and without any explicit resistive term. The radiation field is described through the radiative energy density, its momentum vector (radiation flux) and the photon number density (Sądowski & Narayan 2015). The radiation stress-energy tensor is closed using the M1 closure scheme (Levermore 1984; Sądowski et al. 2013) modified according to Sądowski et al. (2015) to include radiative viscosity.

In this work we improve the physics implemented in KORAL and evolve the electron and ion species independently. Below we discuss some implementation details.

3.1 Adiabatic evolution and viscous dissipation

To estimate the energy dissipation in a given cell during a given time step, we compare the thermal energy in the cell, as obtained via the energy equation, with the thermal energy that is predicted by *purely adiabatic evolution*. The difference between these two quantities reflects the non-adiabatic increase in the internal energy of the gas, i.e, the "viscous" dissipation.

For computing the adiabatic evolution, we use the separate entropy evolution equations of the electrons and ions, viz., (7) and (8), with the right-hand sides set to zero. However, there is a somewhat subtle issue here. Consider the finite-difference version of the adiabatic evolution equation of one of the species in cell i between time n and $n+1$:

$$(\rho s u^t)^{n+1}_i = (\rho s u^t)^n_i - \frac{\Delta t}{\Delta x}\left((\rho s u^x)^n_{i+1/2} - (\rho s u^x)^n_{i-1/2}\right). \tag{50}$$

Here, s is the entropy per particle of the species under consideration, and the fluxes are computed at the cell walls $i\pm1/2$ in the usual way. The above equation states that the entropy content of the cell at time $n+1$ is a linear combination of the old entropy in the cell and new entropy that has flowed into (or out of) the cell. This can equally be written as

$$s^{n+1}_i = \frac{(\rho u^t)^n_i}{(\rho u^t)^{n+1}_i} s^n_i - \frac{\frac{\Delta t}{\Delta x}(\rho u^x)^n_{i+1/2}}{(\rho u^t)^{n+1}_i} s^n_{i+1/2} + \frac{\frac{\Delta t}{\Delta x}(\rho u^x)^n_{i-1/2}}{(\rho u^t)^{n+1}_i} s^n_{i-1/2} \tag{51}$$

$$\equiv f_i s^n_i + f_{i+1/2} s^n_{i+1/2} + f_{i-1/2} s^n_{i-1/2}, \tag{52}$$

where the three f's are the fractions of the final state represented by the three contributing parcels of gas.

Equation (52) is incorrect when we consider finite-sized cells and finite time steps. Whenever two parcels of gas with different properties are mixed together at constant volume, the resulting combined gas will end up in a state whose energy content is given by the sum of the initial energies of the two parcels (energy is conserved), but whose entropy will not be the sum of the entropies of the two initial parcels (entropy is not conserved). In effect, thermal energy will flow from particles of the hotter parcel to those of the cooler parcel, conserving thermal energy, but causing the net entropy to increase.

The relevant question now is the following: Does the entropy increase caused by the transfer of thermal energy between two or more parcels of gas inside a single cell represent viscous dissipation? We think not. This entropy increase is caused by the irreversible process of transfering energy from hot to cold gas within a cell. It takes place merely because our numerical code is unable to keep track of the properties of individual parcels within the cell but is forced to consider a single homogenized fluid. There is no real dissipation involved, i.e., no creation of new thermal energy via shocks or turbulence or magnetic reconnection. In other words: The finite-volume cell-averaging process artificially increases the entropy of a zone. This increase of entropy should not be treated as dissipation.

We further argue that it is the above thermally homogenized fluid, which has enhanced entropy due to thermal mixing, that represents what we call *purely adiabatic evolution* in the first paragraph of this subsection. It is this thermal energy that should be subtracted from the thermal energy obtained via the energy equation to estimate the energy dissipation in the cell. The resulting estimate of the dissipation will be less than the amount we would estimate if we directly took s^{n+1}_i from equation (52) and computed an internal energy from that.

We note yet another complication. Consider for simplicity a single species ideal gas with a constant adiabatic index γ. The entropy per particle of the gas is proportional to $s_1 = \ln(p/\rho^\gamma)$, but sometimes, the quantity $s_2 = p/\rho^{\gamma-1}$ itself is taken as the conserved quantity (e.g., Ressler et al. 2015). Let us imagine that we ignore the entropy of thermal mixing discussed above and estimate the internal energy corresponding to *purely adiabatic evolution* directly from the entropy s^{n+1} in equation (52). The answer we get will be different depending on whether we use s_1 or s_2. The reason is that equation (52) is a linear combination of three entropy terms. However, each entropy term is a non-linear function of the internal energy density u and mass density ρ of the particular gas parcel, and the function is different in the case of s_1 and s_2. As a result, the final estimate of u for the homogenized cell will be different whether we use s_1 or s_2.

The solution to all the above complications is not obvious. Recall that the problem is caused by the fact that, in any numerical scheme, we can keep track of only a limited set of data in each cell, viz., the gas properties at cell centers. Once a piece of gas has crossed into a cell, it loses its individuality and is considered to be mixed homogeneously with the rest. Exactly how should we mix the parcels when defining what we call *purely adiabatic evolution*? We discuss below in §3.1.1 one possible approach that is arguably consistent. We have not used that approach in the work reported in this paper. Here we make the somewhat arbitrary choice of mixing the different parcels at a constant density equal to the final density of the given cell. That is, for each of the three parcels of gas in equation (52), we calculate the internal energy density corresponding to

the *final* rest-mass density of the cell: $\tilde{u}^{n+1}_{i,i\pm1/2} = u(s^n_{i,i\pm1/2}, \rho^{n+1}_i)$. We then linearly sum these final internal energies, using the same mixing fractions f as before,

$$u^{n+1}_i = f_i \tilde{u}^{n+1}_i + f_{i+1/2}\tilde{u}^{n+1}_{i+1/2} + f_{i-1/2}\tilde{u}^{n+1}_{i-1/2}. \quad (53)$$

This is the internal energy that we use as our proxy for "purely adiabatic evolution." Once we have u^{n+1}_i, we then recover the corresponding temperature, $\theta^{n+1}_i = \theta(u^{n+1}_i, \rho^{n+1}_i)$, the entropy per particle, $s^{n+1}_i = s(u^{n+1}_i, \rho^{n+1}_i)$, etc., using the relations discussed in Appendix A. Note that the above calculations are done for each of the two species.

One final detail concerns the entropies and internal energies, $s^n_{i\pm1/2}$, $\tilde{u}^n_{i\pm1/2}$, at the cell boundaries. The natural choice would appear to be

$$s^n_{i\pm1/2} = \frac{(\rho s u^x)^n_{i\pm1/2}}{(\rho u^x)^n_{i\pm1/2}}. \quad (54)$$

However, we have found that even small errors in the numerical reconstructions at the walls lead, because of the exponential dependence of energy density on entropy, to erroneous values of the internal energy density. This in turn often leads to negative temperatures in the final state. To avoid this, we use *upwind* values of the entropy per particle,

$$s^n_{i\pm1/2} = s^n_{\rm upwind}. \quad (55)$$

For example, if gas flows from cell $i-1$ to i, we set $s^n_{i-1/2} = s^n_{i-1}$, while if gas flows from cell i to $i-1$, we set $s^n_{i-1/2} = s^n_i$. Similarly for $s^n_{i+1/2}$. This approach is guaranteed to be stable and, as we discuss below, provides good accuracy.

3.1.1 *A potentially more consistent approach*

An unsatisfactory aspect of the method described above is our decision to mix the individual fluid parcels at constant density. This is computationally very convenient and is the reason we chose it. However, one suspects that there ought to be a physically more consistent approach.

One attractive option is to mix the parcels in such a fashion that the internal energy of the final state is a minimum. Let us suppose that we have N parcels of fluid, each with a mass M_j and entropy S_j. We wish to choose the volumes V_j occupied by the parcels, subject to the condition that they sum up to the total volume V of the cell,

$$\sum_{j=1}^{N} V_j = V. \quad (56)$$

Let the internal energy of each parcel be U_j, which is a function of V_j. We are interested in adjusting the V_j so as to minimize the total internal energy,

$$\sum_{j=1}^{N} U_j \equiv U = \text{minimum}. \quad (57)$$

Using a Lagrange multiplier Λ for the volume constraint, the problem reduces to minimizing

$$\sum_{j=1}^{N} \left(U_j + \lambda V_j\right) = \text{minimum}. \quad (58)$$

Each parcel must thus satisfy the condition

$$\left(\frac{\partial U_j}{\partial V_j}\right)_{S_j} = -\lambda, \quad (59)$$

where we have explicitly noted that each parcel conserves its own entropy (it changes adiabatically) under the volume changes we are considering. From elementary thermodynamics, $(\partial U/\partial V)_S = -P$, where P is the pressure. Thus, the minimum internal energy we seek satisfies

$$P_j = \lambda, \quad (60)$$

i.e., all the fluid parcels have the same pressure (which is equal to λ). The actual value of this pressure is obtained by imposing the volume constraint (56).

While the above "uniform pressure" result is simple and physically appealing, it is not numerically as convenient as the constant density prescription we have used in the present paper. The reason is that the inversion from pressure to volume for a fixed entropy involves a non-linear equation in the quasi-relativistic regime (Appendix A), not to mention that each fluid parcel itself consists of two fluids, ions and electrons, each with its own conserved entropy. Thus, one needs to solve a set of coupled nonlinear equations to compute the constant-pressure minimum-energy state. We intend to explore this in future work.

3.2 Other implementation notes

Within each Runge-Kutta time substep the evolution equations are applied via the following sequence of operations.

(i) The effective adiabatic index of the gas, $\gamma_{\rm gas}$, is calculated through Eq. 28 using the electron and ion temperatures from the end of the previous time step.

(ii) The advective parts (no source terms) of Eqs. 2-5 (total gas) are applied in the standard explicit way (for details of the particular implementation see Sądowski et al. 2013). In the case of Eqs. 7-8 (electron and ion entropy), we follow the procedure described in the previous sub-section.

(iii) At the end of the explicit operator we calculate at each cell the local viscous dissipation rate by comparing the non-adiabatic evolution of the total gas with the adiabatic evolution of electrons and ions using Eq. 14.

(iv) Knowing the electron and ion temperatures, and the magnetic to gas pressure ratio, the fraction of the viscous heating applied to the electrons is calculated according to Eq. 18.

(v) Electron and ion entropies are updated by increasing their energy densities by the corresponding fraction of the energy injected into the gas by the viscous dissipation.

(vi) The effective adiabatic index of the gas, $\gamma_{\rm gas}$, is recomputed using the just obtained species temperatures.

(vii) Steps (iv) to (vi) are iterated three times to allow $\gamma_{\rm gas}$ to converge to the correct value corresponding to the final, heated state of electrons and ions.

(viii) The remaining source terms in Eqs. 2-5 and Eqs. 7-8, i.e., the radiative coupling, G_ν, the photon source term, $\dot{n}$, and the Coulomb coupling, $q^{\rm C}$ are applied through a semi-implicit operator in a way similar to the one described in (Sądowski et al. 2014). Six primitive quantities are iterated to find the final state: energy density and three components of velocity (corresponding to either gas or radiation), photon number density and electron entropy density. At each iteration, the gas density and ion temperature are obtained from the conserved quantity, ρu^t, and energy conservation ($u_{\rm e} + u_{\rm i} = u_{\rm gas}$), respectively.

For the sake of stability, regular limits are applied on the evolved quantities. In particular, neither the electron nor ion temperature is allowed to drop below one percent of the gas temperature (or, equally, for the pure hydrogen, that neither temperature can

exceed 1.99 times the gas temperature). We find that this criterion is very rarely met in the simulations and that this particular choice of the limit does not influence the accretion flow structure. When imposing density floors (which rarely happened for the simulations presented here), we kept the internal energy of electrons and ions fixed to avoid adding any artificial heating.

4 TESTS

In this Section we describe two sets of test problems which verify the implementation of the new physics in the KORAL code, i.e., the treatment of viscous heating and its effect on electrons and ions, and the radiative and Coulomb coupling between electrons, ions, and radiation.

4.1 1D Shock test

We start with a one-dimensional high Mach number shock test problem as described in detail in Ressler et al. (2015). Two fluids move in opposite directions with $|v| = 10^{-3}c$ and collide at $x = 0$. The gas adiabatic index is fixed to $\gamma = 5/3$, while the electron adiabatic index is $\gamma_e = 4/3$ (Ressler et al. 2015 also considered the trivial case $\gamma_e = 5/3$, but we focus here on the more difficult problem). The temperature of the gas is set up to give a Mach number of $\mathcal{M} = 49$. We identify dissipation by following the entropy of the gas (as in Ressler et al. 2015), not the entropies of the species (as we propose in this paper). We choose a resolution of 512 grid cells.

Figure 1 presents the electron to ion energy density ratio profile at a time corresponding to the shock having travelled a distance $\Delta x \approx 0.13$ in arbitrary units. The central part of the plot shows the properties of the shocked fluid. As Ressler et al. (2015) have shown, one should expect $u_e/u_{gas} = 0.379$. Adopting a linear formula for the entropy per particle[1] ($s = p/\rho^\gamma$), we obtain a post-shock $u_e/u_{gas} = 0.406$, within 7% of the correct solution. Using the logarithmic formula ($s = \log p/\rho^\gamma$) and evolving it using equation (50) blindly, we obtain $u_e/u_{gas} = 0.336$ (11% error). Finally, adopting the logarithmic prescription, but evolving it with the modified scheme described in equation (52, sec. 3.1), we get $u_e/u_{gas} = 0.397$ (5% error), which is closest to the correct solution.

4.2 Driven turbulence

To validate our implementation of viscous heating of electrons and ions, we performed a test similar in spirit to the MHD driven turbulence test of Ressler et al. (2015)[2] We set up a uniform medium on a two dimensional plane with gas density, ρ_0, species temperature, $T_{e,0} = T_{i,0} = 10^8$ K, horizontal magnetic field with gas to magnetic pressure ratio $\beta = p_{gas}/p_{mag} = 6$, and initially zero velocities. At every timestep we perturbed the velocities with random, divergenceless, Gaussian velocity perturbations with average power spectrum, $P(|\delta v|^2) \propto k^6 \exp(-8k/k_{peak})$ with characteristic wavevector, k_{peak}, corresponding to half of the computational box, $k_{peak} = 4\pi/L$. The normalization was chosen to provide a saturated rms velocity $v_{rms} \approx 0.08c$. For constructing the perturbation velocity field we followed Dubinski et al. (1995). We also made sure the perturbations did not introduce net momentum by substracting uniformly from all cells the non-zero residual.

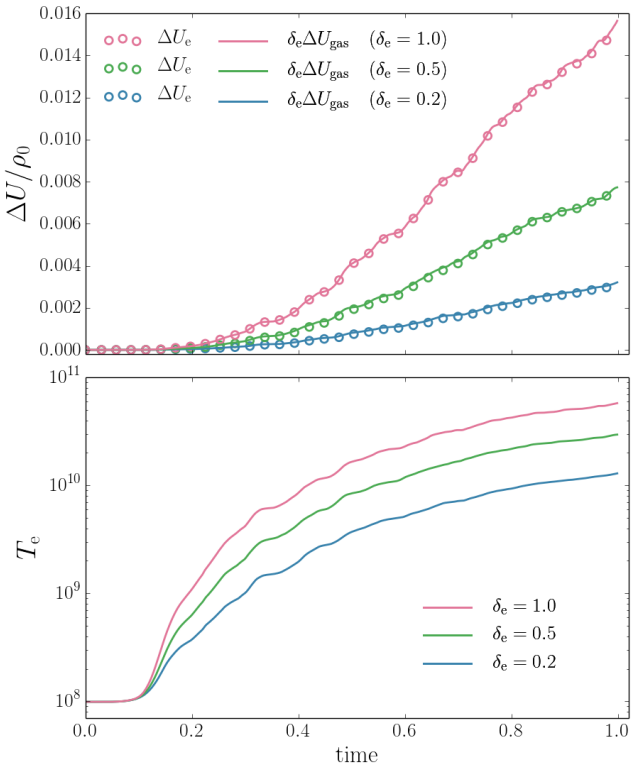

Figure 2. Top panel: Increase of the energy content in electrons in the driven turbulence test (Section 4.2). The colors correspond to three independent runs with different fractions of viscous heating going to electrons: pink, green and blue correspond to $\delta_e = 1.0$, $\delta_e = 0.5$, and $\delta_e = 0.2$, respectively. Circles denote the actual increase of energy of electrons. The solid lines reflect the corresponding fraction of the total gas energy increase. The fact that energy in electrons traces the given fraction of the total energy proves that the viscous heating is applied properly to the different species. Bottom panel: The corresponding increase in the electron temperature. In all cases electrons transition from sub- to relativistic regime. Time is given in arbitrary units.

We performed three independent simulations, each on a two-dimensional grid of 128×128 cells. The random velocity perturbations imposed at every time step introduced kinetic energy into the system which dissipates and contributes finally to the gas thermal energy. As a result, the gas energy content increases with time. Once saturation is reached (i.e., the dissapation rate matches the energy injection rate), the increase is linear.

A fraction, δ_e, of this non-adiabatic heating is deposited in electrons according to Eq. 7. The remaining part goes into ions (Eq. 8). In the top panel of Fig. 2 we show with open circles the increase of the domain-integrated (total) internal energy of electrons (ΔU_e) in the simulations assuming $\delta_e = 1.0$ (pink markers), $\delta_e = 0.5$ (green), and $\delta_e = 0.2$ (blue). This increase is compared with the corresponding fraction of the increase of gas thermal energy ($\delta_e \Delta U_{gas}$), denoted by solid lines. The fact that the internal energy of electrons increases in all three cases at the same rate as the corresponding fraction of the total energy proves that the non-adiabatic viscous heating is identified and applied properly in the code. The bottom panel shows the corresponding increase of the electron temperature. Electrons, initially at 10^8K, heat up and reach

[1] All the formulae adopted for this test are valid only for constant adiabatic indices, in contrast to the more general entropy prescription introduced in this paper.

[2] Our version uses consistent adiabatic indices of gas, ions, and electrons instead of fixing them at predetermined values. We also use a slightly different perturbation magnitude.

Table 1. Parameters of the "gas and radiation box" simulations

Name	$T_{\rm e}$[K]	$T_{\rm i}$[K]	$T_{\rm r}$[K]	T_n[K]	ρ [g cm^{-3}]
ODE1	10^{10}	10^{11}	10^9	10^9	10^{-4}
ODE2	3×10^9	10^{10}	10^9	5×10^8	1
ODE3	10^8	10^8	10^9	10^9	10^{-10}

$\sim 10^{10}$K near the end of the test simulations, transitioning from the sub-relativistic to relativistic regime.

4.3 Radiative and Coulomb coupling of species

We consider an isolated system, a box filled with ions, electrons, and radiation. Assuming that all physical quantities are spatially constant, the only relevant equations are the energy components of Eqs. 3-4, the electron entropy evolution (Eq. 7), and the photon density evolution (Eq. 5). In the absence of dissipative heating these four formulae can be simplified to the following system of ordinary differential equations for the relevant temperatures,

$$\dot{T}_{\rm e} = \frac{m_p(\gamma-1)}{k\rho}\left(\widehat{G^{\rm I}} + q^C\right), \tag{61}$$

$$\dot{T}_{\rm i} = -\frac{m_p(\gamma-1)}{k\rho}q^C, \tag{62}$$

$$\dot{T}_{\rm r} = \frac{\epsilon T_{\rm r}}{\widehat{E}}\left(1-\frac{T_{\rm r}}{T_{\rm e}}\right), \tag{63}$$

$$\dot{T}_n = -\frac{T_n\rho}{3\widehat{E}}\left(\kappa_{\rm P,a}\widehat{E}c - \frac{T_{\rm r}}{T_{\rm e}}\epsilon\right), \tag{64}$$

where we explicitly assumed for simplicity that all the adiabatic indices are fixed and equal γ. The energy coupling term, $\widehat{G^{\rm I}}$, equals,

$$\widehat{G^{\rm I}} = \rho\kappa_{\rm P,a}\widehat{E}c - \epsilon = \rho\left(\kappa_{\rm P,a}\,2.7012kcnT_{\rm r} - 4\sigma\kappa_{\rm P,e}T_{\rm e}^4\right), \tag{65}$$

and the temperature T_n is related to the number density of photons,

$$T_n = \left(\frac{2.7012ck}{4\sigma}n\right)^{1/3} \leqslant T_{\rm r}, \tag{66}$$

and represents the black body temperature corresponding to a given photon density n (if the radiation has a black body spectral energy distribution, then simply $T_n = T_{\rm r}$). We set $\gamma = 5/3$ and account only for bremsstrahlung radiation and Coulomb coupling.

We performed three runs, for which the initial conditions are summarized in Table 1. The evolution of the four temperatures in these simulations is plotted in Fig. 3. For the reference solution we take the accurate results produced by the implicit Runge-Kutta solver (Shampine & Hosea 1996), applied directly to the system of equations 61-64. Fig. 3 indicates that the KORAL code, which solves the corresponding equations in their original form during the semi-implicit operator stage, is able to reproduce the Runge-Kutta solutions with very small error.

5 LOW LUMINOSITY ACCRETION FLOWS

In this Section we describe a series of simulations of low luminosity black hole accretion flows performed with the methods described above. The new physics includes independent evolution of electrons and ions with individual viscous heating, Coulomb coupling and radiative loses, and a sophisticated treatment of radiation

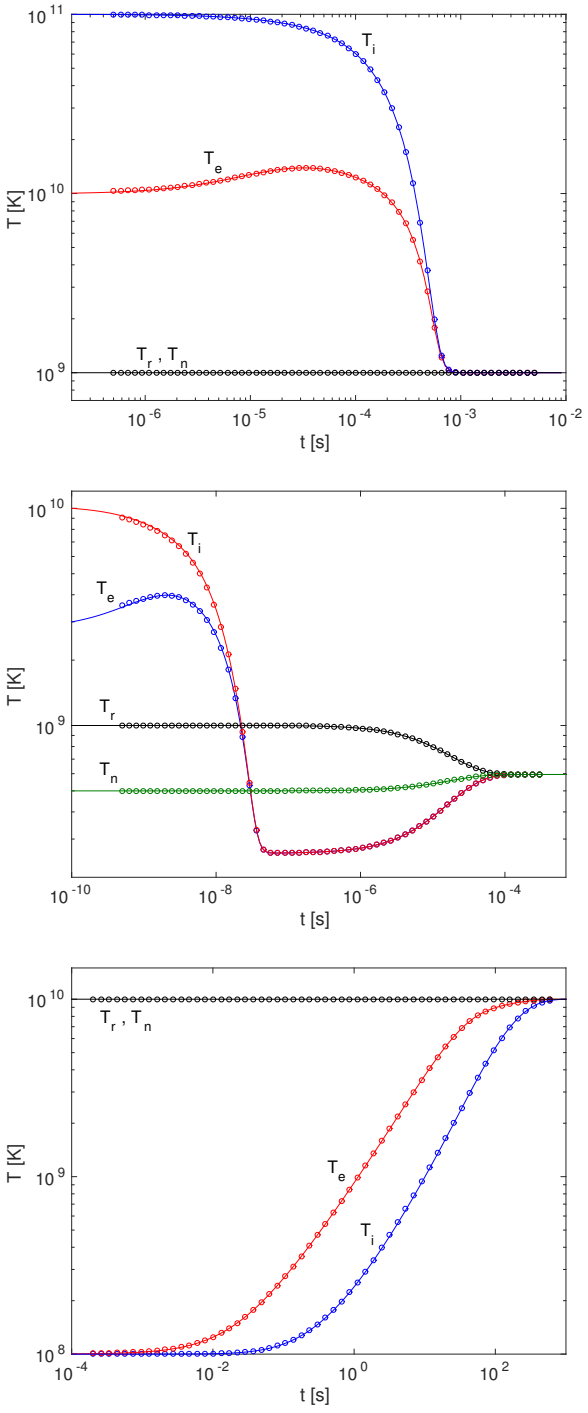

Figure 3. Evolution of the temperatures $T_{\rm e}$, $T_{\rm i}$, $T_{\rm r}$, and $T_{\rm n}$ in the "gas and radiation box" test simulations (Section 4.3). Continuous lines represent results of the Runge-Kutta solver applied directly to Eqs. 61-64, dots represent solutions found with KORAL via its semi-implicit solver. In ODE1 (top) electrons are radiatively cooled and kinetically heated by the hotter ions. In ODE2 (middle) additionally radiation is imbalanced, with $T_{\rm r} > T_{\rm n}$. Because of the large gas density and efficient Coulomb coupling, electrons and ions quickly equilibrate to the same temperature, only later being brought in balance with the radiation. In ODE3 (bottom), the electrons are heated up by absorption of hotter radiation and the collisionally coupled ions follow with a delay. At late times in all three tests, the systems approach thermodynamical equilibrium with $T_{\rm e} = T_{\rm i} = T_{\rm r} = T_{\rm n}$.

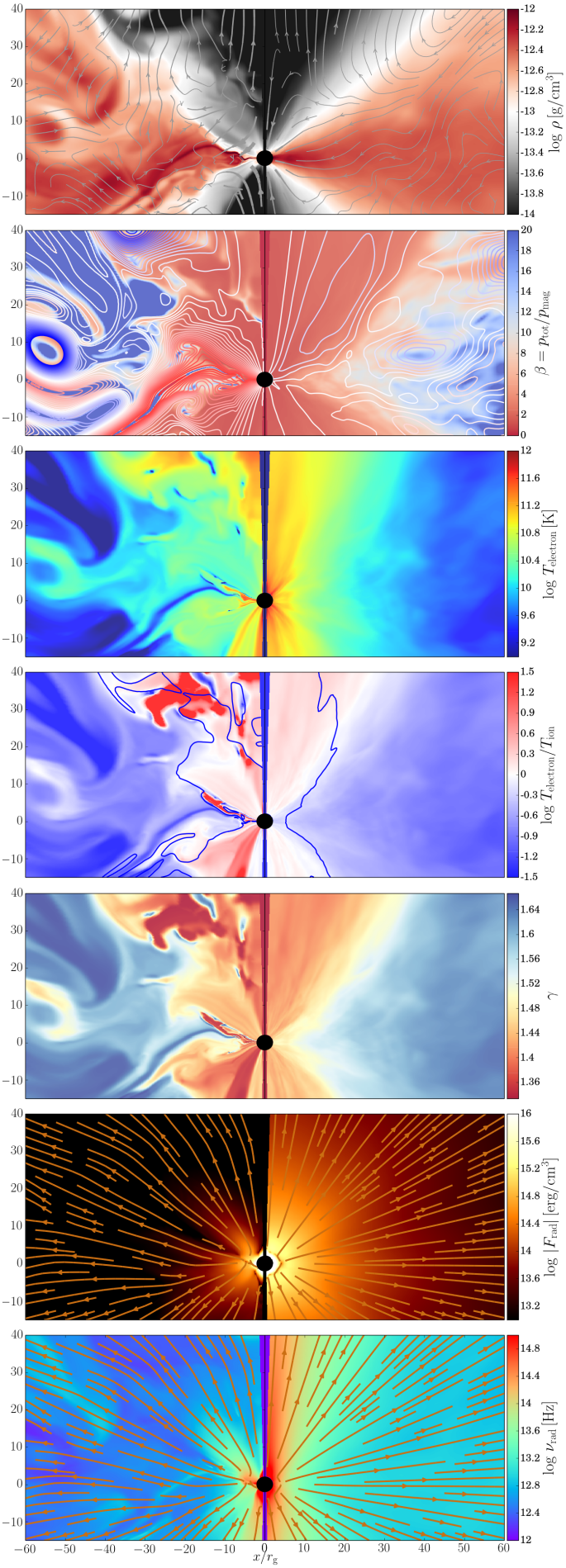

Figure 4. Snapshot (left) and time-averaged (right) distributions of (top to bottom) gas density, magnetization and poloidal magnetic field lines, electron temperature, electron to ion temperature ratio, effective gas adiabatic index, magnitude of the radiative flux, and the characteristic radiation frequency, for model `Rad8`. Streamlines in the topmost and two bottommost panels show the directions of the poloidal velocity and radiative flux, respectively. The blue contours in the fourth panel show where the magnetic pressure equals the gas pressure.

which is coupled to electrons through spectrally integrated free-free and synchrotron opacities, sensitive to the characteristic temperature of the local radiation field. We also distinguish between energy mean (Planck) and Rosseland mean opacity coefficients. All these elements, together with the GR treatment of MHD already implemented in `KORAL`, put us in a position to study the accretion flows with intermediate optical depths.

In this paper we discuss a couple of examples of how the BH mass, radiative cooling, and the treatment of the adiabatic index affect the properties of the accretion flows. In a follow up study we will investigate in detail the transition induced by increasing accretion rate.

5.1 Models

We have simulated five models, the parameters of which are specified in Table 2. In three of these (`Rad8`, `Rad8SMBH`, `Rad4`), the gas was coupled to radiation and experienced radiative losses and the momentum transfer. In the remaining two models (`Hd8`, `Hd8fg`) only the hydrodynamical quantities were evolved and radiative effects were neglected. In all the models we accounted for Coulomb coupling.

We chose $10M_\odot$ as our fiducial BH mass, but one of the models (`Rad8SMBH`) considered a BH of mass $4\times10^6 M_\odot$, roughly corresponding to the mass of the supermassive BH in the center of our Galaxy (e.g., Gillessen et al. 2009).

All but one run simulated accretion flows with an average accretion rate of a few $\times\,10^{-8}\dot{M}_{\rm Edd}$. Simulation `Rad4` is the exception corresponding to a much higher accretion rate of a few $\times\,10^{-4}\dot{M}_{\rm Edd}$.

Two of the simulations (`Hd8` and `Hd8fg`) are non-radiative. They differ from each other in the treatment of the adiabatic index. While the former recalculates the adiabatic index of the gas at each time step and uses the generalized form of entropy as introduced in this work (Appendix A), the latter assumes fixed values of the gas and electron adiabatic indices (5/3 and 4/3, respectively). Correspondingly, the dissipation is obtained from the entropy of the total gas, not from the entropies of the individual species. This corresponds to the method adopted in Ressler et al. (2015).

5.2 Numerical setup

Every simulation was performed in the Kerr-Schild metric and assumed a non-rotating BH. We restricted ourselves to axisymmetry and applied the fiducial model of the mean-field dynamo from Sądowski et al. (2015) to prevent the axisymmetric magnetic field from decaying. We used spherical-like coordinates and adopted a resolution of 384x384x1 cells in radius, polar angle and azimuth, respectively. The radial cells were distributed exponentially in radius, with the innermost cell located inside the BH horizon at $r = 1.85r_{\rm g}$. The polar cells were uniformly distributed.

All the simulations except the high accretion rate `Rad4` were initialized with the same torus in hydrostatic equilibrium. The parameters of the torus were set following Narayan et al. (2012). In particular, the inner edge of the torus was located at $10r_{\rm g}$, which, for the given angular momentum profile, resulted in a hot and geometrically thick structure.[3] The torus was threaded with multiple loops

[3] We note that it is essential to start simulations of optically thin flows with a hot and thick torus. Otherwise, the gas may not have enough time (which is limited by the viscous timescale) to reach the correct local equilibrium temperature (equal roughly to the virial temperature) before falling into the

of a weak (contributing at most to 3% of the gas pressure) magnetic field with loop properties identical to the ones adopted in Narayan et al. (2012). The density of the gas in the torus was chosen by adjusting the torus entropy parameter (Penna et al. 2013) to provide the required accretion rate. The torus was initially surrounded by a a non-rotating atmosphere of negligible mass.

At the onset of the simulations we set the electron and ion temperatures equal to the gas temperature (which may not be a good assumption if Coulomb coupling is ineffective and the particles are not evolved long enough to forget the initial state). The radiation field both inside and outside the torus was initiated with a negligible energy density and radiation temperature of 10^5 K.

To start the higher accretion rate simulation `Rad4` we chose a different approach and took a very early stage of simulation `Rad8`, rescaled the density and magnetic field pressure up by four orders of magnitude (keeping all the temperatures constant), and evolved it from there. Such an approach is advantageous for higher accretion rates, where the large optical depth requires non-negligible radiation pressure inside the torus, and starting with a virtually empty radiation field would not be a good approximation.

5.3 Properties of the models

5.3.1 Fiducial model

In Fig. 4 we show properties of the fiducial model `Rad8` corresponding to a $10M_\odot$ BH accreting at a very low accretion rate of $\sim 4\times10^{-8}\dot{M}_{\rm Edd}$, and emitting $\sim 2\times10^{-9}L_{\rm Edd}$[4]. Such a system can represent a transient BH X-ray binary in deep quiescence, in between the outbursts. We chose such a low accretion rate for the fiducial model to verify whether radiative cooling is important for accretion rates comparable with those characterizing the accretion on Sgr A*. The impact of the accretion rate, BH mass, and radiative feedback is studied via the remaining simulations.

The left and right halves of Fig. 4 show for the fiducial model the distributions in the poloidal plane obtained from a snapshot (corresponding to $t = 15000t_{\rm g}$) and time-averaged over $t = 10000t_{\rm g}$ – $20000t_{\rm g}$, respectively. The top-most panel shows the distribution of gas density (colors) and the velocity field (streamlines). The disk is evidently thick and turbulent. On average, the gas flows towards the BH in the equatorial region. Outflows emerge from the surface layers outside $r \approx 20r_{\rm g}$.

The second panel shows the magnetization parameter $\beta = p_{\rm tot}/p_{\rm mag}$ with magnetic field lines overplotted (blue and red contours correspond to clockwise- and counter-clockwise poloidal magnetic field). Note that the instantaneous magnetic field is turbulent. The amount of the magnetic flux that has accumulated at the horizon is far below the magnetically arrested limit (Narayan et al. 2003; Tchekhovskoy et al. 2011) because of the initial magnetic field setup of alternating polarity which causes the loops subsequently accreted onto the BH to reconnect with the magnetic flux already present in the inner region. The polar region, where the gas density is the lowest, is highly magnetized ($\beta < 1$). The bulk of the disk, on the other hand, is dominated by gas pressure ($\beta > 1$). The magnetization level at the equatorial plane increases towards the BH from $\beta \approx 10$ at $30r_{\rm g}$ to $\beta \approx 5$ at $15r_{\rm g}$. The global picture of the gas dynamics resembles well the optically thin accretion flows obtained numerically in past simulations (e.g., Narayan et al. 2012).

The third panel in Fig. 4 shows the electron temperature obtained by consistently evolving electrons during the simulation. In the fiducial model the electrons were dragged with the gas, underwent adiabatic evolution, were affected by a fraction of the viscous heating (Section 2.2.2), exchanged energy with the ions through Coulomb interactions (Section 2.2.3), and cooled by emitting radiation (Section 2.3.2). As will turn out later, for such a low accretion rate and gas density, radiative feedback and Coulomb coupling are negligible. The left half of the third panel shows the instantaneous distribution of electron temperature. Electrons are coldest far from the BH and in the bulk of the disk – at $r \approx 50$ their temperature does not exceed 10^{10} K. They heat up on the way towards the BH, mainly because of adiabatic compression. The viscous heating is weak near the equatorial plane where the magnetic pressure is sub-dominant and most of the heating goes into the ions. In the polar region, on the contrary, the magnetic field is strong and as a result most of the viscous heating goes into the electrons (as per our heating sub-grid model, Eqs. 18 & 19). In the instantaneous temperature profile, electron filaments are evident at $\sim 10^{11.5}$ K overlapping with the regions of strongest magnetization. Such hot electrons enter the polar region and strongly contribute to the time-averaged properties (shown in the right half of the panel), covering the entire polar region with hot electrons with an average temperature of 10^{11} K.

The fourth panel in Fig. 4 shows the electron to ion temperature ratio. The two species compete in how much dissipative heating goes into each. In regions where the magnetic pressure dominates over the gas pressure (in our case this corresponds to the polar region), most of the heating goes into the electrons (Eqs. 18 & 19). In the opposite case, where the magnetic pressure is sub-dominant (in the bulk of the disk), the ions are heated more efficiently. In addition to viscous heating, electrons and ions exchange energy in Coulomb collisions. We also account for radiative cooling which affects only electrons. In the case of the fiducial model, the electron/ion temperature balance is determined mostly by the sub-grid viscous heating prescription (Eq. 18, Section 6.1) which determines the fraction of heating going into each of the species as a function of their temperatures and local magnetization. In regions dominated by the magnetic pressure, electrons are heated more efficiently than ions. If gas pressure dominates (e.g., near the equatorial plane), ions receive most of the dissipated heat. As a result, the two regions can be distinguished. In the bulk of the disk, where magnetic pressure is sub-dominant and reflects the saturated state of MRI, ions are hotter than electrons ($T_{\rm e}/T_{\rm i} \approx 0.2$ near $20r_{\rm g}$). In the polar region, on the contrary, electrons carry more energy per particle and $T_{\rm e}/T_{\rm i} \approx 2$. The boundary between the two regions agrees well with the surface where the magnetic pressure equals the gas pressure, $p_{\rm mag} = p_{\rm gas}$ (compare the contour lines in the right half of the fourth panel in Fig. 4).

The electron temperature exceeds $10^{9.5}$K virtually everywhere inside $r = 50r_{\rm g}$. Therefore, electrons are relativistic and their equation of state can be characterized by the adiabatic index, $\gamma_{\rm int\,e} = 4/3$. Ions, on the other hand, never exceed $10^{11.5}$K, which, keeping in mind their much larger mass, makes them non-relativistic ($\gamma_{\rm int\,i} \approx 5/3$) everywhere. The effective adiabatic index of the electron and ion mixture depends on both temperatures (Eq. 28) and is not dominated by the more massive ions (ions and electrons at the same temperature carry the same energy per particle). The fifth panel in Fig. 4 shows the effective adiabatic index of the total gas,

BH. This would not be an issue if we could start the gas far from the BH, as in real systems in nature. However, because of computational limitations, the accreting gas in simulations has to be initialized relatively close to the BH.

[4] This is manifestly a radiative inefficient accretion flow (or ADAF), since a radiatively efficient flow at this accretion rate would have a luminosity of $\sim 4\times10^{-8}L_{\rm Edd}$, i.e. 20 times larger.

Table 2. Model parameters

Name	$M/M_\odot$	$\dot{M}_{\rm BH}/\dot{M}_{\rm Edd}$	$L/L_{\rm Edd}$	adiabatic index
`Rad8`	10	4.4×10^{-8}	2.1×10^{-9}	consistent
`Rad8SMBH`	4×10^{6}	1.9×10^{-8}	4.6×10^{-10}	consistent
`Rad4`	10	4.5×10^{-4}	3.8×10^{-4}	consistent
`Hd8`	10	4.4×10^{-8}	N/A	consistent
`Hd8fg`	10	3.2×10^{-8}	N/A	$\gamma_{\rm gas}=5/3$, $\gamma_{\rm inte}=4/3$

Other parameters: $a_*=0$, $r_{\rm in}=1.85r_{\rm g}$, $r_{\rm out}=1000r_{\rm g}$. Resolution:384x384x1
Accretion rate and luminosity measured at $r=20r_{\rm g}$.

$\gamma_{\rm gas}$. In the polar region, where electrons are the hottest and most relativistic, the electron/ion mixture effectively follows $\gamma_{\rm gas}\approx4/3$. In the bulk of the disk, on the other hand, where the electrons are only moderately relativistic, the adiabatic index of the gas is significantly higher, $\gamma_{\rm gas}\approx1.55$. Therefore, assuming a single fixed value for the gas adiabatic index for the whole domain is probably not a good approximation.

The methods described in this paper allow for simulating the parallel evolution of the gas and the radiation field. The latter is generated self-consistently by the gas which cools by emitting bremsstrahlung and synchrotron radiation. Subsequently, the emitted photons only interact with the gas they are penetrating if the gas's optical depth is large enough, which can lead to the exchange of energy and momentum. In the two bottom-most panels of Fig. 4 we show the properties of the radiation field generated by gas in the fiducial model `Rad8` ($10M_\odot$, non-rotating BH, $\sim3\times10^{-8}\dot{M}_{\rm Edd}$). The second panel from the bottom shows the magnitude of the radiative flux (colors) and its direction in the poloidal plane (streamlines). Radiation propagates outward almost isotropically. This reflects the fact that the gas is optically thin and its distribution does not affect the propagation of photons. Most of the flux comes from the innermost, hottest, and densest region, where synchrotron emission is most efficient. The integrated radiation flux gives a luminosity on the order of $\sim10^{-9}L_{\rm Edd}$.

The last panel in Fig. 4 shows the characteristic temperature of the emitted radiation. At such low accretion rates, virtually all of the photons are synchrotron photons and carry energies corresponding to frequencies 10^{13} Hz – 10^{14} Hz (for a $10M_\odot$ BH). The angular distribution of photon energies is not isotropic, in contrast to the radiative flux distribution. The most energetic photons are generated in the polar region (because of highest electron temperatures there) and tend to propagate upward. Colder electrons, closer to the equatorial plane, generate less energetic photons. Radiative postprocessing is required to obtain more detailed information on the emerging electromagnetic spectrum.

5.3.2 *Parameter study*

In this Section we study how the choice of the adiabatic index, radiative feedback, BH mass, and accretion rate affect the properties of low-luminosity accretion flows.

Figure 5 compares the gas density (top), electron temperature (middle), and electron to ion temperature ratio (bottom panels) distributions for the five models we have simulated.

Let us first compare model `Hd8` (first column) with the fiducial simulation `Rad8` (third column). The former was initiated with exactly the same equilibrium torus as the latter, and adopted the same generalized entropy prescription, which allows for a consistent adjustment of the adiabatic index in the course of the simulation. In contrast to the fiducial model, however, it did not evolve the radiation field, so that radiative cooling by electrons was neglected. As a comparison of the panels of density, electron temperature, and temperature ratio in Fig. 5 shows, the properties of the two models are virtually indistinguishable. This shows that, at such a low accretion rate ($\sim4\times10^{-8}\dot{M}_{\rm Edd}$), the impact of radiation on the accretion flow properties is negligible.

Model `Hd8fg` (second column in Fig. 5) was initiated from the same initial state, but the adiabatic indices of the total gas and the electrons were not adjusted according to the local ion and electron temperatures. Instead, the respective adiabatic indices were fixed at $\gamma_{\rm gas}=5/3$ and $\gamma_{\rm inte}=4/3$. In addition, the dissipation was identified by comparing adiabatic and non-adiabatic evolution of the total gas, not the particular species. This approach turns out to give qualitatively similar results for the properties of the accretion flow. In particular, the electron temperatures are quite close. Only the density distributions show slight differences, as may be expected for gas evolving under different equations of state.

The fourth column in Fig. 5 corresponds to model `Rad8SMBH` which is similar to the fiducial model `Rad8`, but the BH mass is different and roughly matches that of the supermassive BH in the center of our galaxy. The initial torus of gas in `Rad8SMBH` had the same dynamical properties as in `Rad8`, but the density of the gas was scaled to provide a comparable accretion rate in Eddington units. The top panels in columns 3 and 4 compare the gas density distributions. In the case of model `Rad8SMBH`, the real densities were rescaled by the ratio of the BH masses and the accretion rates, so that the color scale can be matched between the panels. Both the density distribution and the electron/ion temperatures (shown in the second and third rows) almost exactly correspond to each other. This, once again, proves that radiative feedback does not affect accretion flows at such low accretion rates, independent of the BH mass.

The properties of the radiation field, however, are different in models `Rad8` and `Rad8SMBH`. The more massive BH in `Rad8SMBH` results in a larger radiative luminosity (which still corresponds to roughly the same Eddington fraction), and a different electromagnetic spectrum. For low-luminosity accretion flows, as discussed so far, radiation is dominated by synchrotron emission. The characteristic frequency of the emitted radiation (Eq. B23) depends on the strength of the magnetic field and the square of the electron temperature. While the latter is independent of BH mass (as long as radiative cooling is weak), the strength of the magnetic field scales as $1/\sqrt{M_{\rm BH}}$. Thus, one expects the peak frequency in the electromagnetic spectrum for model `Rad8SMBH` to be roughly two orders of magnitude lower. As Fig. 6 shows, this is, indeed, the case. The fiducial model ($M_{\rm BH}=10M_\odot$, left panel) emits radiation with characteristic frequencies around 10^{14} Hz and 10^{13} Hz near the axis and in the equatorial plane, respectively. Model `Rad8SMBH` ($M_{\rm BH}=4\times10^{6}M_\odot$, middle panel), on the other hand, produces less energetic photons and the spectrum is expected to peak near $10^{11.5}$

Hd8	Hd8fg	**Rad8**	Rad8SMBH	Rad4
$4.4 \times 10^{-8} \dot{M}_{\rm Edd}$	$3.2 \times 10^{-8} \dot{M}_{\rm Edd}$	$4.4 \times 10^{-8} \dot{M}_{\rm Edd}$	$1.9 \times 10^{-8} \dot{M}_{\rm Edd}$	$\sim 3.5 \times 10^{-4} \dot{M}_{\rm Edd}$
$10 M_\odot$	$10 M_\odot$, $\gamma_{\rm gas} = \frac{5}{3}$, $\gamma_{\rm int\,e} = \frac{4}{3}$	$10 M_\odot$	$4 \times 10^6 M_\odot$	$10 M_\odot$

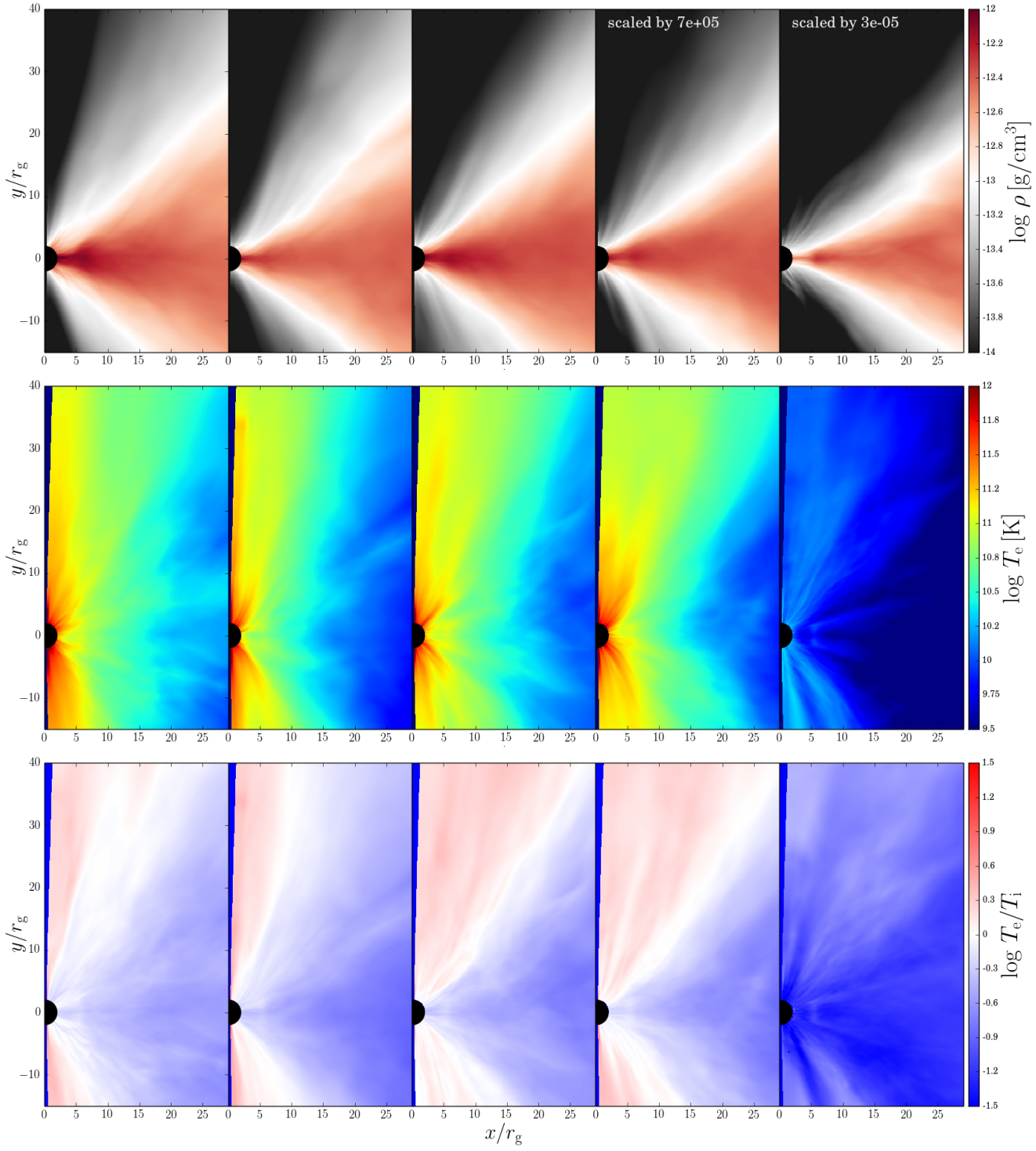

Figure 5. Time-averaged distribution of logarithms of density (top), electron temperature (middle) and electron to ion temperature ratio (bottom) for (left to right) models `Hd8`, `Hd8fg`, `Rad8`, `Rad8SMBH`, and `Rad4`.

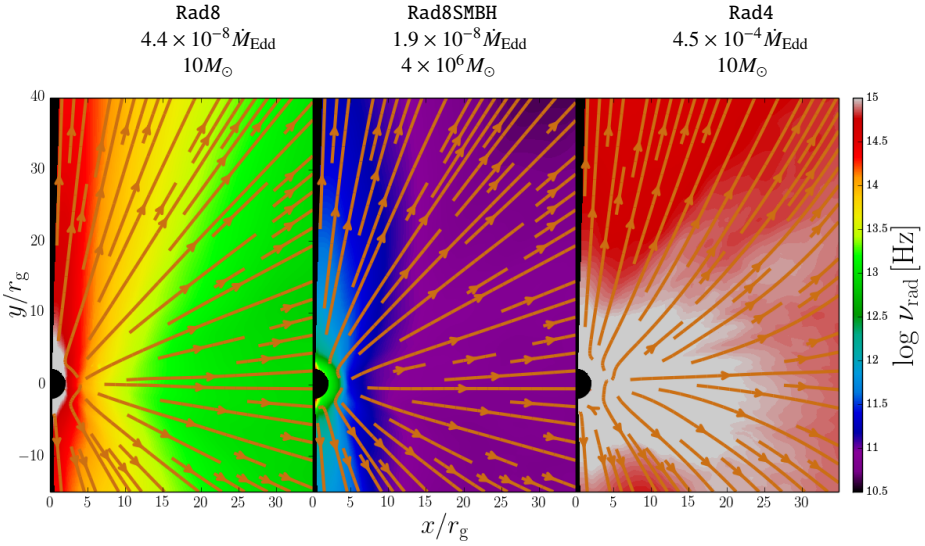

Figure 6. Characteristic frequency of emitted radiation for models (left to right) `Rad8`, `Rad8SMBH`, and `Rad4`.

and $10^{10.5}$ Hz, respectively. It is remarkable that these are roughly the frequencies where the synchrotron emission from Sgr A* peaks (Yuan et al. 2003), which proves that our algorithm, despite using a grey approximation, is able to track the temperature of radiation reasonably well.

Finally, we compare the fiducial model `Rad8` with model `Rad4`, which was designed to correspond to an accretion rate roughly 4 orders of magnitude larger, i.e., $\sim 10^{-4} \dot{M}_{\rm Edd}$. This model was initialized from an early stage of the fiducial simulation, after rescaling the density up by four orders of magnitude (keeping magnetic to gas pressure ratio and all the temperatures fixed). Once the density was rescaled, the radiative cooling immediately started to affect the electrons. This effect is clearly seen in the rightmost column in Fig. 5. There are noticeable differences between model `Rad4` and all the other simulations discussed so far – the disk is confined to a thinner region near the equatorial plane, and the gas is much colder than in the previous, low accretion rate models. The temperature at the equatorial plane is as low as 10^9K at $15 r_{\rm g}$. These distinct properties result from thermal cooling of an initially thick and hot accretion disk.

6 DISCUSSION

6.1 Electron temperatures

The final electron temperature depends on the initial temperature (both in the temporal and spatial sense), and the amount of dissipation that the electrons undergo. If the amount of energy added by dissipation is much smaller than the initial internal energy, then the final temperature of the electrons will differ from the original only by the adiabatic compression term. If, on the contrary, the amount of the dissipation is much larger than the original energy content of electrons then the initial state is quickly forgotten.

Our simulations of low-luminosity accretion flows show that the latter is the case. In particular, the gas density in the inner region is very close to constant (Fig. 5), and therefore adiabatic compression does not modify the thermal energy as the gas moves towards the BH. However, the gas temperature shows a steep $\sim 1/R$ variation with radius, which implies that the thermal energy must increase ten-fold when crossing a decade in radius. Thus, the initial energy content is quickly forgotten and it is the dissipated energy (magnetic or kinetic) that heats up the gas as it flows in. This is in contrast to the properties of self-similar, $\gamma = 5/3$, models of ADAFs (Narayan & Yi 1995) which predict no dissipation at all.

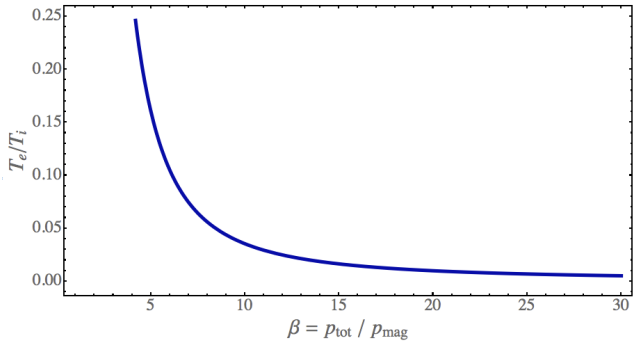

Figure 7. Electron to ion temperature ratio corresponding to the equilibrium state (eq. 68) for given magnetization parameter β as implied by the Howes (2010) heating prescription. See Section 6.1 for details.

This fact has significant consequences. In particular, assuming $\gamma_{\rm e} = 4/3$ and $\gamma_{\rm i} = 5/3$, in the limit of dissipation dominating, one finds that the final electron to ion temperature ratio is given by,

$$\frac{T_{\rm e}}{T_{\rm i}} = \frac{1}{2} \frac{\delta_{\rm e}}{1 - \delta_{\rm e}}, \tag{67}$$

where $\delta_{\rm e}$ is the fraction of the dissipated energy going into the electrons.

The heating prescription adopted in this work (Section 2.2.2) gives δ_e as a function of the magnetization parameter, $\beta = p_{\rm tot}/p_{\rm mag}$, and the electron to ion temperature ratio, $T_{\rm e}/T_{\rm i}$. There is an equilibrium value of this ratio for which applying viscous heating does not modify the temperature distribution. This equilibrium ratio is given through,

$$\left(\frac{T_{\rm e}}{T_{\rm i}}\right)_{\rm eq} = \frac{1}{2} \frac{\delta_{\rm e}\left((T_{\rm e}/T_{\rm i})_{\rm eq}, \beta\right)}{1 - \delta_{\rm e}\left((T_{\rm e}/T_{\rm i})_{\rm eq}, \beta\right)}. \tag{68}$$

Figure 7 shows the equilibrium temperature ratio as a function of the magnetization parameter. It is evident that this ratio depends strongly on the gas magnetization parameter, e.g., it equals 0.066 and 0.243 for $\beta = 10$ and 5, respectively. The magnetization of our fiducial model near $r = 20r_{\rm g}$ is close to $\beta = 5$, and the value of $(T_{\rm e}/T_{\rm i})_{\rm eq}$ predicted for this magnetization is indeed close to the one obtained in the simulation (0.2, see Fig. 5).

Shearing box simulation with no vertical magnetic field have shown that the magnetic field saturates near $\beta = 10$. However, inclusion of even a small amount of net vertical flux can drive this parameter down substantially (Bai & Stone 2013). Such a behavior has been shown to affect global simulations as well (e.g., Narayan et al. 2003; Sadowski 2016).

One should keep in mind the implicit relation betwen magnetization and electron temperature (eq. 68) when interpreting and comparing results of simulations initiated with different configurations of the magnetic field. Likewise, this strong dependence could be used in the future to infer the properties of the magnetic field in accretion disks from their observed radiative properties.

We should also mention that, ultimately, three-dimensional simulations will be needed to verify that the axisymmetric, dynamo-based models presented here capture the heating rates accurately.

6.2 Implemented and not implemented physics

Our code KORAL evolves the accretion flow under the magneto-hydrodynamical (MHD) approximation, i.e., we treat electrons and ions as fluids characterized by their own, isotropic, pressures. In reality, electrons and ions are particles moving in self-generated magnetic and electromagnetic fields, and are expected to undergo plasma instabilities. Under the adopted MHD approximation we effectively assume that all these instabilities saturate such that the total gas and its individual species (electrons and ions) can be reasonably well described by an isotropic pressure and adiabatic indices, with appropriate distinctions between $\gamma_{\rm CV}$ and $\gamma_{\rm int}$ (see Appendix A). This, however, does not have to be the case (see Sharma et al. 2007, and voluminous literature on collisionless plasmas). Whether or not this fluid approximation works has to be verified in the future by using a microscale particle approach in the global context of an accretion disk.

In grid-based codes like KORAL, kinetic and magnetic energy is dissipated into thermal energy on the grid scale through numerical dissipation. As long as energy is conserved, such an approach gives the proper dissipative (viscous) heating of the gas. However, if one wants to distinguish electrons from ions, it becomes crucial to know how much of the dissipated energy goes into each species, which is determined on microscales, far below the resolution. In this work, following Ressler et al. (2015), we adopted the sub-grid prescription of Howes (2010) which is based on theoretical models of the dissipation of MHD turbulence in almost collisionless plasmas and to some extent validated by numerical experiments. It is still, however, only an approximation and could be avoided once hybrid algorithms, combining the particle and global frameworks, become feasible. What is more, one should in principle allow also for non-thermal, relativistic electron population, which may not change the overall dynamics of the two-phase accretion flow, but may be relevant to the generated radiation.

Energy can be transported in many ways. We account for a number of them, including, in particular, radiative transport and the exchange of energy between gas and the radiation field. We ignore, however, anisotropic heat conduction along magnetic field lines. The effect of this mechanism on optically thin accretion flows has recently been studied by Ressler et al. (2015), Chandra et al. (2015), and Foucart et al. (2016). Ressler et al. (2015), in particular, have shown that the anisotropic heat conduction contributes to at most 20% of the isotropic heat flux. The low efficiency of the anisotropic conduction results from the fact that the magnetic field in accretion disks is predominantly toroidal and there are no significant temperature gradients in that direction. The same authors, however, claim that it might be better to set the conduction parameter to $\alpha_{\rm e} \approx 10$ as the resulting heat flux corresponds better to that expected in collisionless plasmas.

Finally, we mention a set of caveats not specific to the algorithm presented in this work, but applicable also to standard, single-fluid, radiative simulations. We adopt the ideal-MHD approximation, i.e., we implicitly assume that the resistivity is so low that there is no electric field in the comoving frame of the gas. Such an assumption is reasonable as long as we deal with a fully ionized, hot gas, which is the case for astrophysical BH accretion disks. We do not include explicitly the resistive term. However, magnetic reconnection still takes place due to numerical, grid-scale resistivity. One may wonder if numerical resistivity impacts the rate at which the magnetic field is advected onto the BH which depends on the effective Prandl number. In most MHD accretion flows the Prandtl number is dominated by the turbulent component and therefore not sensitive to microscopic (neglected by us) resistivity (Guan & Gammie 2009).

We treat the radiation transport in an approximate way. First, we solve it in the grey approximation, imposing a diluted black body shape for the spectrum, though we do use consistent grey opacities for bremsstrahlung and synchrotron processes. As long as the spectrum is dominated by a single component (either synchrotron, Compton or free-free), our approximation is reasonable. However, one should be careful when two of the emission mechanisms contribute to the spectrum at a similar level. Our assumption of a diluted black body shape would mix the two components into one and the resulting opacities would not be correct. Fortunately, in low-luminosity accretion flows synchrotron emission always dominates, and one may expect that the transition to bremsstrahlung and Comptonization with increasing accretion rate would be rapid enough not to cause any trouble. Finally, we adopt the M1 closure scheme (Levermore 1984; Sądowski et al. 2014) which describes the shape of the local radiation field with just four numbers: its energy density and three spatial components of momentum. Obviously, it has its limitations, especially when handling multiple sources of radiation. This is not, however, a serious concern in optically thin, low-luminosity accretion flows, where most of the emission comes from the inner region and propagates isotropically outward (see the last-but-one panel in Fig. 4) which the M1 closure can handle reasonably well.

6.3 Uncertainities and limits

In this work we have presented five simulations designed to help assess the importance of particular factors on accretion flow properties. We studied the impact of radiative cooling at two, very different, accretion rates, the impact of fixing adiabatic indices to constant values, and finally, the importance of the BH mass. This set, however, does not exhaust the parameter space. Most importantly, the properties of an accretion flow, especially in the polar region, are known to depend on the large scale topology of the magnetic field. In particular, if the magnetic field exhibits uniform polarity on long timescales, then the magnetic field deposited on the BH and

accumulated on the axis may dynamically affect the flow dynamics forming a so-called magnetically arrested disk (MAD, Narayan et al. 2003; Tchekhovskoy et al. 2011). For rotating BHs this can result in efficient jet production. In a similar way, the magnetization of gas, and in turn, the heating of electrons and their radiative properties, would be affected. All the simulations discussed in this work were initialized with the same magnetic field setup. We plan to study other initial field configurations in the future.

The most exciting application of the numerical methods developed here is to study in detail the transition from totally optically thin accretion flows towards geometrically thin but optically thick disks. One has to be aware, however, of the difficulties related to simulating the latter. The standard thin disk model Shakura & Sunyaev (1973) predicts that at accretion rates on the order of $10^{-2}\dot{M}_{\rm Edd}$, the expected disk thickness is $H/R \sim 0.01$. To resolve the fastest growing MRI mode, this disk thickness has to be resolved by at least a few dozens of cells. This introduces a very demanding criterion for vertical resolution and time step. In addition, geometrically thin disks evolve on very long viscous time scales, $t_{\rm vis} \approx (R/H)^2/\alpha\Omega_{\rm K}$. For obvious reasons, the duration of simulations is limited, and therefore one cannot hope to obtain an equilibrium solution for a thin disk covering a large range of radii. Last but not least, there is the issue of thermal stability which kicks in when portions of a thin disk become radiation pressure dominated ($\sim 0.1\dot{M}_{\rm Edd}$), which seems to require a strong magnetic field for stabilization (Sadowski 2016). All these factors will require special attention when studying the transition in detail.

6.4 Comparison with previous studies

In this Section we discuss the relation of our work to some of the related works published in recent years.

6.4.1 *Ressler et al. (2015)*

In Ressler et al. (2015) the authors introduced a method of evolving electrons in GR magnetohydrodynamical (MHD) simulations. We follow their approach and adopt the same sub-grid prescription (Howes 2010) for the fraction of dissipation going into electrons. The authors account for anisotropic heat conduction along magnetic field lines which we ignore, as they found it is always sub-dominant. Their approach, however, adopts a number of simplifications which we have avoided. Firstly, their electrons are decoupled from the evolution of the gas, i.e., they evolve electrons only during the postprocessing stage and the electrons do not affect the dynamics of the gas. Secondly, they assumed fixed adiabatic indices of gas and electrons throughout the simulations. This last assumption is not generally accurate – the effective adiabatic index of the gas cannot be approximated by $\gamma_{\rm gas} = 5/3$, instead, a consistent value, dependent on the instantaneous and local electron and ion temperatures, should be used. However, in practice, the difference is not large, and simulations run with fixed $\gamma_{\rm gas}$ do produce qualitatively similar results as simulations that use a more accurate variable γ, at least in the case of hot accretion flows with low $\dot{M}$. Ressler et al. (2015) also neglect radiative cooling and feedback, as well as Coulomb coupling. This is a valid approximation for accretion rates much less than $10^{-8}\dot{M}_{\rm Edd}$, but it cannot be used for rates much larger than this.

6.4.2 *Dibi et al. (2012)*

The critical accretion rate above which radiation cooling becomes important and affects properties of the accretion flow was the topic of another study – Dibi et al. (2012). The authors implemented simplified radiative transfer in GR MHD simulations (following Esin et al. 1996), and, in this way, were able for the first time to include radiative cooling. They found that, as long as the accretion rate is below $6 \times 10^{-8}\dot{M}_{\rm Edd}$ (in our units, note the different definition of the Eddington accretion rate adopted in their work), radiative effects are negligible. Our fiducial model (`Rad8`), accreting at a level of $3 \times 10^{-8}\dot{M}_{\rm Edd}$, is unaffected by radiative cooling, in contrast to the high accretion rate model (`Rad4`), showing significant radiative feedback. Both conclusions are consistent with the findings of Dibi et al. (2012). We will determine the exact value of the critical accretion rate in a future work.

Let us, however, point out differences between the two works. In terms of the electron evolution and radiative transfer, our work supersedes Dibi et al. (2012) in all aspects. Instead of adopting, as they did, a local cooling based on local gas properties and an estimate of the temperature scale height, we evolve the radiation field simultaneously and in the whole domain (although using an approximated closure scheme). Instead of fixing the electron to ion temperature ratio throughout the computational box, we calculate the two temperatures consistently. We also do not fix the adiabatic index of the gas. We will have to perform a more extensive parameter study to assess how well the critical accretion rate obtained with our code agrees with the predictions of Dibi et al. (2012).

6.4.3 *Wu et al. (2016)*

Numerical methods for approximate treatment of radiation similar to Dibi et al. (2012) have been adopted recently in Wu et al. (2016), although the authors used a Newtonian MHD code. Similarly to Dibi et al. (2012), the electron temperature was arbitrarily prescribed. The main point of interest of Wu et al. (2016) was the state transition taking place at accretion rates of the order $\sim 10^{-2}\dot{M}_{\rm Edd}$. The authors have identified the formation of cold and dense clumpy/filamentary structures embedded within the hot gas, which, when the accretion rate becomes sufficiently high, gradually merge and settle down onto the mid-plane. Their findings are in good agreement with what we found for our high-accretion rate model `Rad4`. We point out, however, that our methods supersede the approach adopted both in Dibi et al. (2012) and Wu et al. (2016), allowing for simulating the transitional regime more reliably. We plan to verify findings of these works in future studies.

6.4.4 *Ohsuga et al. (2009) and Ohsuga & Mineshige (2011)*

Last but not least, we mention earlier works by Ohsuga et al. (2009) and Ohsuga & Mineshige (2011) who for the first time reproduced three distinct modes of accretion flows (hot and thick, thin and slim) within radiation-magnetohydrodynamic simulations. The authors adopted simplified radiation treatment (flux-limited diffusion), including only free-free and bound-free opacities, and did not distinguish electron and gas temperatures. Their setup was sufficient to qualitatively simulate the three accretion modes. However, it would not be enough for the purpose of calculating observables.

6.5 From simulations to observables

The algorithm presented here allows for precise tracking of gas evolution and its interaction with the radiation field. The latter is evolved in an approximate way – under the grey approximation, imposing a diluted black body spectral shape and adopting the M1 closure scheme. Therefore, neither the local shape of the radiation field (angular distribution of specific intensities), nor the electromagnetic spectrum is known. From the simulation output, one can only directly recover the amount of energy carried by the radiation field and its characteristic temperature.

To obtain the most interesting observable, i.e., the electromagnetic spectrum for an observer located at a given inclination angle, radiative postprocessing is necessary. For optically thin flows, i.e., for the lowest accretion rates, Monte Carlo techniques (e.g., Shcherbakov et al. 2012; Dexter et al. 2010; Chan et al. 2015a) are most efficient. However, when a geometrically thin and optically thick disk emerges, a grid-based approach may be more adequate (Narayan et al. 2016). One should also take into account that time-averaged and axisymmetric output is not appropriate for calculating the spectrum (Chan et al. 2015a,b). Future work in this direction will therefore require full three-dimensional simulations.

7 SUMMARY

In this paper we have introduced a state-of-the-art algorithm which allows for parallel evolution of gas and radiation field in general relativity, and which evolves electrons and ions independently, consistently tracking their temperatures. Such a method allows for the first time to study the transition from optically thin to optically thick accretion flows, relevant for many AGN and the hard-to-soft transition of X-ray binaries.

The new components of the method, when compared with existing radiation-MHD algorithms, include:

(i) Electron and ion energy contents are evolved through their corresponding entropy conservation equations, modified by source terms including viscous heating, Coulomb coupling and radiative heating or cooling.

(ii) The viscous dissipation is distributed between electrons and ions according to the sub-grid prescription of Howes (2010).

(iii) The adiabatic indices of each species and their mixture are adjusted consistently based on their temperatures.

(iv) The radiative spectrum is described as a diluted black body with, independently evolved, characteristic temperature.

(v) Bremsstrahlung and synchrotron grey opacities are obtained by integration over frequencies consistent with the assumed diluted black body spectral shape. Energy mean Planck opacities are distinguished from the flux mean Rosseland opacities. The latter are used in the momentum exchange term.

We simulated five models of black hole accretion at very low and moderately low accretion rates to assess the impact and importance of various factors. We find that radiative effects are unimportant for gas properties and gas dynamics in the case of a simulation with accretion rate $\sim 4 \times 10^{-8} \dot{M}_{\rm Edd}$. However, in a model with four orders of magnitude larger accretion rate, the radiative cooling does become important – the gas temperature decreases significantly, and a colder, geometrically thinner structure forms, though it is still not quite a classic thin disk. The precise critical accretion rate above which radiative cooling is strong enough to cause the accretion flow to collapse to a geometrically thin disk remains to be determined, and will be the subject of a future study.

8 ACKNOWLEDGEMENTS

We thank Sean Ressler, Martin Rees, Chris Fragile and Charles Gammie for comments on the manuscript. AS acknowledges support for this work by NASA through Einstein Postdoctotral Fellowship number PF4-150126 awarded by the Chandra X-ray Center, which is operated by the Smithsonian Astrophysical Observatory for NASA under contract NAS8-03060. AS thanks Harvard-Smithsonian Center for Astrophysics for its hospitality. RN was supported in part by NSF grant AST 1312651 and NASA grant TCAN NNX 14AB7G. The authors acknowledge computational support from NSF via XSEDE resources (grant TG-AST080026N), from NASA via the High-End Computing (HEC) Program through the NASA Advanced Supercomputing (NAS) Division at Ames Research Center, and from the PL-Grid Infrastructure. AS acknowledges support from the International Space Science Institute. This research was supported by the Polish NCN grant UMO-2013/08/A/ST9/00795. MW acknowledges support of the Foundation for Polish Science within the START programme.

REFERENCES

Abbott, B. P., Abbott, R., Abbott, T. D., et al. 2016, Physical Review Letters, 116, 061102
Abramowicz, M. A., Czerny, B., Lasota, J. P., & Szuszkiewicz, E. 1988, ApJ, 332, 646
Bai, X.-N., & Stone, J. M. 2013, ApJ, 767, 30
Biretta, J. A., Stern, C. P., & Harris, D. E. 1991, AJ, 101, 1632
Blandford, R. D., & Begelman, M. C. 1999, MNRAS, 303, L1
Buchler J. R., & Yueh W. R., 1976, ApJ, 210, 440
Chan, C.-K., Psaltis, D., Özel, F., Narayan, R., & Sądowski, A. 2015, ApJ, 799, 1
Chan, C.-k., Psaltis, D., Özel, F., et al. 2015, ApJ, 812, 103
Chandra, M., Gammie, C. F., Foucart, F., & Quataert, E. 2015, ApJ, 810, 162
Chandrasekhar, S. 1939, *Introduction to the Study of Stellar Structure, Chapter* 10 (Chicago: University of Chicago Press; reprinted New York: Dover Publications)
Dexter, J., Agol, E., Fragile, P. C., & McKinney, J. C. 2010, ApJ, 717, 1092
Dibi, S., Drappeau, S., Fragile, P. C., Markoff, S., & Dexter, J. 2012, MNRAS, 426, 1928
Dubinski, J., Narayan, R., & Phillips, T. G. 1995, ApJ, 448, 226
Esin, A. A., Narayan, R., Ostriker, E., & Yi, I. 1996, ApJ, 465, 312
Foucart, F., Chandra, M., Gammie, C. F., & Quataert, E. 2016, MNRAS, 456, 1332
Fragile, P. C., Olejar, A., & Anninos, P. 2014, ApJ, 796, 22
Gammie, C. F., McKinney, J. C., & Tóth, G. 2003, ApJ, 589, 444
Gillessen, S., Eisenhauer, F., Fritz, T. K., et al. 2009, ApJ, 707, L114
Guan, X., & Gammie, C. F. 2009, ApJ, 697, 1901
Hawley, J. F. 2000, ApJ, 528, 462
Howes, G. G. 2010, MNRAS, 409, L104
Jiang, Y.-F., Stone, J. M., & Davis, S. W. 2014, ApJ, 796, 106
Kalemci, E., Dinçer, T., Tomsick, J. A., et al. 2013, ApJ, 779, 95
Levermore, C. D. 1984, J. Quant. Spectrosc. Radiative Transfer, 31, 149
Mahadevan R., Narayan R., & Yi I., 1996, ApJ, 465, 327
McKinney, J. C., Tchekhovskoy, A., & Blandford, R. D. 2012, MNRAS, 423, 3083
McKinney, J. C., Tchekhovskoy, A., Sadowski, A., & Narayan, R. 2014, MNRAS, 441, 3177
Mignone, A., & McKinney, J. C. 2007, MNRAS, 378, 1118
Mihalas, D., & Mihalas, B. W. 1984, New York, Oxford University Press, 1984, 731 p.

Mościbrodzka, M., Falcke, H., Shiokawa, H., & Gammie, C. F. 2014, A&A, 570, A7
Narayan, R., & Yi, I. 1995, ApJ, 452, 710
Narayan, R., Igumenshchev, I. V., & Abramowicz, M. A. 2003, PASJ, 55, L69
Narayan, R., Tchekhovskoy, A., & McKinney, J. 2010, Accretion and Ejection in AGN: a Global View, ASPC, 427, 127
Narayan, R., Kumar, P., & Tchekhovskoy, A. 2011, MNRAS, 416, 2193
Narayan, R., Sądowski, A., Penna, R. F., & Kulkarni, A. K. 2012, MNRAS, 426, 3241
Narayan, R., Zhu, Y., Psaltis, D., & Saądowski, A. 2016, MNRAS, 457, 608
Ohsuga, K., Mineshige, S., Mori, M., & Kato, Y. 2009, PASJ, 61, L7
Ohsuga, K., & Mineshige, S. 2011, ApJ, 736, 2
Paczynski B. 1983, ApJ, 267, 315
Penna, R. F., Kulkarni, A., & Narayan, R. 2013, A&A, 559, A116
Ressler, S. M., Tchekhovskoy, A., Quataert, E., Chandra, M., & Gammie, C. F. 2015, MNRAS, 454, 1848
Ryan, B. R., Dolence, J. C., & Gammie, C. F. 2015, ApJ, 807, 31
Rybicki, G. B., & Lightman, A. P. 1979, New York, Wiley-Interscience
Sądowski, A., Narayan, R., Tchekhovskoy, A., & Zhu, Y. 2013, MNRAS, 429, 3533
Sądowski, A., Narayan, R., McKinney, J. C., & Tchekhovskoy, A. 2014, MNRAS, 439, 503
Sądowski, A., Narayan, R., Tchekhovskoy, A., Abarca, D., Zhu, Y., & McKinney J. C. 2015, MNRAS, 447, 49
Sądowski, A., & Narayan, R. 2015, MNRAS, 454, 2372
Service, A. T. 1986, ApJ, 307, 60
Sadowski, A. 2016, arXiv:1601.06785
Shakura, N. I., & Sunyaev, R. A. 1973, A&A, 24, 337
Shampine, L. F. & Hosea, M. E. 1996, Applied Numerical Mathematics 20, 21
Sharma, P., Quataert, E., Hammett, G. W., & Stone, J. M. 2007, ApJ, 667, 714
Shcherbakov, R. V., Penna, R. F., & McKinney, J. C. 2012, ApJ, 755, 133
Stepney, S., & Guilbert, P. W. 1983, MNRAS, 204, 1269
Taub, H. 1948, Phys. Rev., 74, 328
Tchekhovskoy, A., Narayan, R., and McKinney, J. C. 2010b, New Astron., 15, 749–754
Tchekhovskoy, A., Narayan, R., & McKinney, J. C. 2011, MNRAS, 418, L79
Weldon, H. A., 1994, Phys. Rev. D, 49, 1579
Wu, M.-C., Xie, F.-G., Yuan, Y.-F., & Gan, Z. 2016, MNRAS,
Yuan, F. 2003, ApJ, 594, L99
Yuan, F., Quataert, E., & Narayan, R. 2003, ApJ, 598, 301
Yuan, F., & Narayan, R. 2014, ARA&A, 52, 529

APPENDIX A: ADIABATIC INDEX AND ENTROPY

The pressure p and internal energy $u_{\rm int}$ of a single-species, non-degenerate, relativistic gas with number density n and temperature T are given by (e.g., Chandrasekhar, S. 1939),

$$p = nkT, \tag{A1}$$

$$u_{\rm int} = \rho c^2 \left(\frac{[3K_3(1/\theta) + K_1(1/\theta)]}{4K_2(1/\theta)} - 1 \right) \tag{A2}$$

$$\equiv \frac{p}{(\gamma_{\rm int} - 1)}, \tag{A3}$$

where $\rho = nm$ is the mass density, m is the particle mass, $\theta = kT/mc^2$ is the dimensionless temperature, $K_n(x)$ is the modified Bessel function of order n, and we have defined an effective adiabatic index $\gamma_{\rm int}$ associated with $u_{\rm int}$. The internal energy has a series expansion of the form,

$$u_{\rm int} = nkT \left(\frac{3}{2} + \frac{15}{8}\theta - \frac{15}{8}\theta^2 \ldots \right), \tag{A4}$$

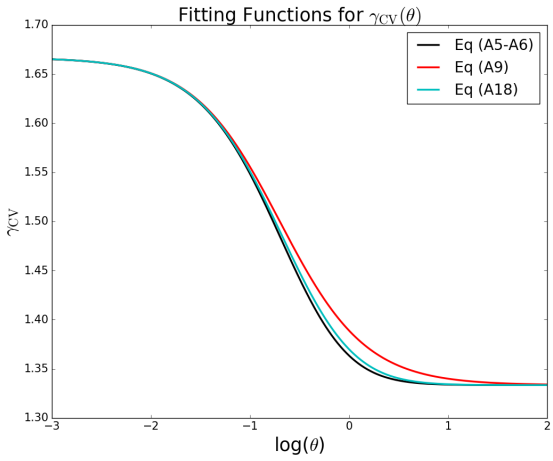

Figure A1. Comparison of the exact solution for $\gamma_{\rm CV}$ as a function of the dimensionless temperature θ, obtained from equations (A5), (A6), with two approximate expressions given in equations (A9) and (A18). We use equation (A9) in the present work.

asymptoting to $(3/2)nkT$ in the non-relativistic limit ($\theta \to 0$) and $3nkT$ in the ultrarelativistic limit ($\theta \to \infty$). Correspondingly, the adiabatic index $\gamma_{\rm int}$ asymptotically approaches 5/3 and 4/3 in the two limits.

The specific heat at constant volume C_V and its corresponding adiabatic index $\gamma_{\rm CV}$ are given by

$$C_V = \frac{du_{\rm int}}{dT}$$

$$= \frac{nk}{8\theta^2} \left(\frac{3K_4(1/\theta) + 4K_2(1/\theta)) + K_0(1/\theta)}{K_2(1/\theta)} - \frac{3K_3^2(1/\theta) + 4K_3(1/\theta)K_1(1/\theta) + K_1^2(\theta)}{K_2^2(1/\theta)} \right) \tag{A5}$$

$$\equiv \frac{nk}{\gamma_{\rm CV} - 1}. \tag{A6}$$

The adiabatic index $\gamma_{\rm CV}$ has a series expansion,

$$\gamma_{\rm CV} = \frac{5}{3} - \frac{5}{3}\theta + \frac{20}{3}\theta^2 \cdots, \tag{A7}$$

and it again asymptotically approaches to 5/3 and 4/3, respectively, as $\theta \to 0$ and ∞. Finally, the specific heat at constant pressure C_P satisfies

$$C_P = C_V + nk = \gamma_{\rm CV} C_V. \tag{A8}$$

Above, we have been careful to distinguish between $\gamma_{\rm int}$ and $\gamma_{\rm CV}$. These two effective adiabatic indices are in general not equal to each other; they match only in the two asymptotic limits, $\theta \to 0$ and $\theta \to \infty$.

While the above expressions are exact, they are not convenient for numerical computations because of the presence of the Bessel functions. They are also not easy to "invert" to solve for the temperature, given either the internal energy or the entropy. We therefore look for simple approximations that are better suited for computations.

We begin with $\gamma_{\rm CV}$. Our philosophy is to find a function that matches the first two terms in the series expansion (A7) and also satisfies the asymptotic result $\gamma_{\rm CV} \to 4/3$ as $\theta \to \infty$. One conve-

nient function is

$$\gamma_{\rm CV} \approx \frac{5+20\theta}{3+15\theta}. \tag{A9}$$

Figure A1 compares this approximation with the exact result (eqs. A5, A6). We see that the approximation is very good for small values of θ up to about 0.1 and also at large θ above a few tens. In between, the agreement is not as good, but probably acceptable. As discussed in the main text, our simulations generally have non-relativistic ions with $\theta_i \sim 0.01 - 0.1$ and relativistic electrons with $\theta_e > 10$. For these temperature ranges, the approximation (A9) is quite good.

We now use equation (A9) to derive an approximate expression for the entropy s per particle:

$$Tds = \frac{C_V}{n}dT + pdv = \frac{k}{(\gamma_{\rm CV}-1)}dT - \frac{kT}{\rho}d\rho, \tag{A10}$$

where v is the volume per particle. Using equation (A9) for $\gamma_{\rm CV}$ and integrating, this gives

$$s \approx k \ln\left[\frac{\theta^{3/2}\left(\theta+\frac{2}{5}\right)^{3/2}}{\rho}\right] + C, \tag{A11}$$

where C is the integration constant. The main advantage of this approximate formula is that, for given s and ρ, it can be easily inverted to calculate the temperature. Ignoring the integration constant C (which is equivalent to making a specific choice for the zero-point of the entropy), we obtain

$$\theta \approx \frac{1}{5}\left(\sqrt{1+25\left[\rho\exp\left(\frac{s}{k}\right)\right]^{2/3}} - 1\right). \tag{A12}$$

We also need an approximation for $u_{\rm int}$. One option is to substitute (A9) in the following equation,

$$\frac{du_{\rm int}}{dT} = C_V = \frac{nk}{\gamma_{\rm CV}-1}, \tag{A13}$$

and to integrate. This gives

$$u_{\rm int} \approx \rho c^2\left[3\theta - \frac{3}{5}\ln\left(1+\frac{5}{2}\theta\right)\right]. \tag{A14}$$

Given $u_{\rm int}$ and ρ, this transcendental equation can be solved iteratively for θ; the solution generally converges quickly. As explained below, we have followed this method in some test runs.

For computational speed, it is often useful to have a formula for $u_{\rm int}$ that can be be inverted analytically. For this, we employ the same philosophy as we used for $\gamma_{\rm CV}$, viz., we look for a simple approxmation of $u_{\rm int}$ which behaves correctly in the two asymptotic limits, $\theta \to 0$, $\theta \to \infty$, and also fits the second term in the Taylor series (A4). Such a function is the following,

$$u_{\rm int} \approx \rho c^2 \frac{\theta(6+15\theta)}{(4+5\theta)}, \tag{A15}$$

which inverts to give,

$$\theta \approx \frac{1}{30}\left(-6 + 5\frac{u_{\rm int}}{\rho c^2} + \sqrt{36+180\frac{u_{\rm int}}{\rho c^2}+25\left(\frac{u_{\rm int}}{\rho c^2}\right)^2}\right). \tag{A16}$$

The above approximation for $u_{\rm int}$ can be written in terms of the effective adiabatic index $\gamma_{\rm int}$ (cf, eq. A3),

$$\gamma_{\rm int} \approx \frac{10+20\theta}{6+15\theta}, \quad u_{\rm int} \equiv \frac{p}{\gamma_{\rm int}-1}. \tag{A17}$$

This form of $\gamma_{\rm int}$ was previously used by Narayan et al. (2011).

For completeness, if we take the approximation (A15) for $u_{\rm int}$ and substitute it in (A13), we obtain the following expression for $\gamma_{\rm CV}$,

$$\gamma_{\rm CV} \approx \frac{20\,(2+8\theta+5\theta^2)}{3\,(8+40\theta+25\theta^2)}, \tag{A18}$$

which agrees very well with the exact result for $\gamma_{\rm CV}$ (Fig. A1). However, this expression involves the ratio of quadratic factors of θ, and it does not give an analytically invertible solution for the entropy s (the inversion again involves a transcendental equation). It is therefore less useful than equations (A9), (A11), (A12), (A16).

We have run tests in which we used equation (A9) for $\gamma_{\rm CV}$, (A11) for s and (A12) for computing θ from s, and tried two different approaches for inverting $u_{\rm int}$. In the first approach, we numerically inverted equation (A14) to obtain θ for a given value of $u_{\rm int}$, while in the second, we used the approximate inversion formula (A16). The two methods gave virtually identical results. We therefore used the second method in the simulations discussed in the paper.

We note one final inconsistency: our approximations do not satisfy Taub's inequality (Taub 1948; Mignone & McKinney 2007). However, we believe this is not a serious concern.

APPENDIX B: OPACITIES AND EMISSIVITIES

The frequency dependent opacities κ_ν are related to the frequency dependent emissivities, ϵ_ν with the Kirchhoff's law,

$$\kappa_\nu(\nu, T_{\rm e}) = \frac{\epsilon_\nu(\nu, T_{\rm e})}{4\pi\rho\widehat{B}_\nu(\nu, T_{\rm e})}, \tag{B1}$$

where $\widehat{B}_\nu$ is a spectral radiance of a black body,

$$\widehat{B}_\nu(\nu, T) = \frac{2h\nu^3}{c^2}\frac{1}{\exp(h\nu/kT)-1}. \tag{B2}$$

In the notation that we adopt, opacities κ_ν are expressed in units of area per mass. It is often convenient to give formulas for opacity times gas density, which is in units of inverse length. Mean (grey) opacities are obtained by averaging κ_ν over ν with proper weights. Clearly, there is no single choice of weights that would preserve all the physical properties of a frequency-resolved κ_ν (Mihalas & Mihalas 1984).

In global simulations of accretion flows the Rosseland mean is commonly adopted,

$$\kappa_{\rm R} \equiv \kappa_{\rm R}(T_{\rm e}, T_{\rm r}) = \frac{\int_0^\infty \frac{\partial\widehat{E}_\nu(\nu,T_{\rm r})}{\partial T_{\rm r}}d\nu}{\int_0^\infty \kappa_\nu^{-1}(\nu, T_{\rm e})\frac{\partial\widehat{E}_\nu(\nu,T_{\rm r})}{\partial T_{\rm r}}d\nu}, \tag{B3}$$

where $\widehat{E}_\nu(\nu, T_{\rm r})$ denotes the radiation spectral energy distribution at a given time and location. Under our simplifying assumptions we have $\widehat{E}_\nu(\nu, T_{\rm r}) \propto \widehat{B}_\nu(\nu, T_{\rm r})$, i.e., $\widehat{E}_\nu(\nu, T_{\rm r})$ corresponds to a diluted black body spectrum, see Section 2.3.

The Rosseland mean properly addresses conservation of momentum in an optically thick gas. We employ it exclusively in the momentum equations by designing a numerical fit to Eq. B3.

The energy equation coupling term, $\widehat{G}^{\prime}$ (Eq. 31), consists of emission and absorption terms, for which the energy mean opacities are employed,

$$\kappa_{\rm P,e} \equiv \kappa_{\rm P,e}(T_{\rm e}, T_{\rm r}) = \frac{\int_0^\infty \kappa_\nu(\nu, T_{\rm e})\widehat{B}_\nu(\nu, T_{\rm e})d\nu}{\int_0^\infty \widehat{B}_\nu(\nu, T_{\rm e})d\nu}, \tag{B4}$$

$$\kappa_{\rm P,a} \equiv \kappa_{\rm P,a}(T_{\rm e}, T_{\rm r}) = \frac{\int_0^\infty \kappa_\nu(\nu, T_{\rm e})\widehat{E}_\nu(\nu, T_{\rm r})d\nu}{\int_0^\infty \widehat{E}_\nu(\nu, T_{\rm r})d\nu}. \quad \text{(B5)}$$

The emission energy mean opacity (Planck opacity) $\kappa_{\rm P,e}$ is weighted with the black body spectral energy density distribution characterized by the electron temperature, $T_{\rm e}$. It recovers the total emission from radiating electrons, i.e.,

$$\epsilon_{\rm tot} \equiv \int_0^\infty \epsilon_\nu(\nu, T_{\rm e})\, d\nu = \kappa_{\rm P,e}\rho\, 4\pi\widehat{B}. \quad \text{(B6)}$$

The absorption mean opacity is weighted with the radiation spectral energy distribution $\widehat{E}_\nu(\nu, T_{\rm r})$, in our case corresponding to the diluted black body spectrum. Under such an assumption, this is equivalent to averaging κ_ν with the Planck distribution, $\widehat{B}_\nu(\nu, T_{\rm r})$, at a radiation temperature $T_{\rm r}$. The absorption mean energy opacities depend on both electron and radiation temperatures. As $T_{\rm r} \to T_{\rm e}$, we find that $\kappa_{\rm P,a} \to \kappa_{\rm P,e}$.

In the equation for the photon density evolution, Eq. 5 and Eq. 47, we use yet another mean opacity - the number mean opacity $\kappa_{\rm n}$, weighted with the spectral density of the photon number density

$$\widehat{n}_\nu = \frac{\widehat{E}_\nu(\nu, T_{\rm r})}{h\nu}, \quad \text{(B7)}$$

hence,

$$\kappa_{\rm n} \equiv \kappa_{\rm n}(T_{\rm e}, T_{\rm r}) = \frac{\int_0^\infty \kappa_\nu(\nu, T_{\rm e})\widehat{E}_\nu(\nu, T_{\rm r})\nu^{-1}d\nu}{\int_0^\infty \widehat{E}_\nu(\nu, T_{\rm r})\nu^{-1}d\nu}. \quad \text{(B8)}$$

We now give the spectrally resolved emmisivity and opacity coefficients for the bremsstrahlung and synchrotron processes, from which mean opacities can be calculated using Eqs. B3 - B8. For computational reasons the improper integrals that define mean opacities need to be approximated using numerical fits, given in Eqs. 38 - 45 as well as further in this appendix.

B1 Bremsstrahlung

Using the notation from Section 2.4, bremsstrahlung frequency dependent emissivity is equal to (Rybicki & Lightman 1979)

$$\epsilon_\nu^{\rm (ff)} = 6.8\times10^{-38} T_{\rm e}^{-1/2}\overline{n}n_{\rm e}\overline{g}\, R(T_{\rm e}) \exp\left(-h\nu/kT_{\rm e}\right)\left[\frac{\rm erg}{\rm cm^3\,s\,Hz}\right], \quad \text{(B9)}$$

from which we find the integrated total emissivity

$$\epsilon^{\rm (ff)} = 1.4\times10^{-27} T_{\rm e}^{1/2}\overline{n}n_{\rm e}\overline{g}\, R(T_{\rm e})\left[\frac{\rm erg}{\rm cm^3\,s}\right], \quad \text{(B10)}$$

The spectrally resolved opacity coefficient is found using Kirchhoff's law,

$$\kappa_\nu^{\rm (ff)}\rho = 3.7\times10^{8} T_{\rm e}^{-1/2}\overline{n}n_{\rm e}\overline{g}\, R(T_{\rm e})\frac{1-\exp(-h\nu/kT_{\rm e})}{\nu^3}[\rm cm^{-1}Hz^{-1}]. \quad \text{(B11)}$$

Inserting Eq. B11 into Eqs. B4-B5 and substituting $x = h\nu/kT_{\rm e}$, we find the energy mean opacities

$$\kappa_{\rm P,e}^{\rm (ff)}\rho = 3.7\times10^{8}\overline{n}n_{\rm e}\overline{g}\, R(T_{\rm e})T_{\rm e}^{-7/2}\left(\frac{h}{k}\right)^3\frac{I_1}{I_2}$$
$$= 6.2\times10^{-24}\overline{n}n_{\rm e}\,\overline{g}\, R(T_{\rm e})T_{\rm e}^{-7/2}, \quad \text{(B12)}$$

$$\kappa_{\rm P,a}^{\rm (ff)}\rho = 3.7\times10^{8}\overline{n}n_{\rm e}\overline{g}\, R(T_{\rm e})T_{\rm e}^{-7/2}\left(\frac{h}{k}\right)^3\xi^{-4}\frac{I_3(\xi)}{I_2}$$
$$= \kappa_{\rm P,e}^{\rm (ff)}\rho\xi^{-4}I_3(\xi) \approx \kappa_{\rm P,e}^{\rm (ff)}\rho\xi^{-3}\cdot 1.047\ln(1+1.6\xi). \quad \text{(B13)}$$

The dimensionless parameter ξ corresponds to temperatures ratio $\xi = T_{\rm r}/T_{\rm e}$. Using Eqs. B10 and B12 it is easy to verify that $\epsilon^{\rm (ff)} = \kappa_{\rm P,e}^{\rm (ff)}\rho 4\sigma T_{\rm e}^4$. Subsequently, the Rosseland mean opacity is calculated with Eq. B3,

$$\kappa_{\rm R}^{\rm (ff)}\rho = 3.7\times10^{8}\overline{n}n_{\rm e}\overline{g}\, R(T_{\rm e})T_{\rm e}^{-7/2}\left(\frac{h}{k}\right)^3\frac{I_4}{I_5(\xi)}$$
$$= \kappa_{\rm P,e}^{\rm (ff)}\rho\xi^{-3}I_2\frac{I_4}{I_5(\xi)} \approx \kappa_{\rm P,e}^{\rm (ff)}\rho\xi^{-3}\cdot 14.12 f_{\rm R}(\xi), \quad \text{(B14)}$$

where

$$f_{\rm R}(\xi) = \left(432.7 - 106.8\xi^{-3/5} + 43.17\xi^{-4/5} + 57.88\xi^{-1}\right)^{-1}. \quad \text{(B15)}$$

The accuracy of the numerical fits given by Eqs. B13 - B14 is indicated in Fig. B1. The relevant integrals used in Eqs. B12-B14 are

$$I_1 = \int_0^\infty \frac{1-\exp(-x)}{\exp(x)-1}dx = 1, \quad \text{(B16)}$$

$$I_2 = \int_0^\infty \frac{x^3}{\exp(x)-1}dx = \frac{\pi^4}{15}, \quad \text{(B17)}$$

$$I_3(\xi) = \int_0^\infty \frac{1-\exp(-x/\xi)}{\exp(x)-1}dx \approx \xi^{-1}\ln(1+1.6\xi), \quad \text{(B18)}$$

$$I_4 = \int_0^\infty \frac{x^4\exp(x)}{[\exp(x)-1]^2}dx = \frac{4\pi^4}{15}, \quad \text{(B19)}$$

$$I_5(\xi) = \int_0^\infty \frac{(x/\xi)^7\exp(x/\xi)d(x/\xi)}{[\exp(x/\xi)-1]^2[1-\exp(-x)]} \approx \frac{11.95}{f_{\rm R}(\xi)}. \quad \text{(B20)}$$

In the case of the bremsstrahlung radiation, integral B8 diverges, indicating that an infinite number of low-energy photons are generated. This divergence can be regularized with a more detailed treatment of the collective plasma effects, see, e.g., Weldon (1994). In this work, for the sake of simplicity, we substitute the photons absorption opacity with the energy absorption mean opacity,

$$\kappa_{\rm n}^{\rm (ff)} \equiv \kappa_{\rm P,a}^{\rm (ff)}. \quad \text{(B21)}$$

We estimate the number of the emitted photons by dividing the total energy produced in the bremsstrahlung process by the (black body) mean emitted photon energy,

$$\widehat{n}_{\rm ff} = \frac{\epsilon^{\rm (ff)}}{\langle h\nu\rangle} = \frac{\kappa_{\rm P,e}^{\rm (ff)}\rho 4\pi\widehat{B}}{2.7012kT_{\rm e}}. \quad \text{(B22)}$$

B2 Synchrotron

We follow Mahadevan et al. (1996) and Esin et al. (1996) who give the ultrarelativistic gas synchrotron emissivity in Gaussian-cgs units as

$$\epsilon_\nu^{\rm (sy)} = 4.43\times10^{-30}4\pi\nu_M n_{\rm e}\frac{x_M I'(x_M)}{2\theta_{\rm e}^2}\left[\frac{\rm erg}{\rm cm^3\,s\,Hz}\right], \quad \text{(B23)}$$

where

$$x_M = \frac{\nu}{\nu_M}, \qquad \nu_M = \frac{3}{2}\frac{eB}{2\pi m_{\rm e}c}\theta_{\rm e}^2 = 1.19\times10^{-13}BT_{\rm e}^2\ [\rm Hz]. \quad \text{(B24)}$$

$I'(x_M)$ is a fitting function provided by Mahadevan et al. (1996),

$$I'(x_M) = \frac{4.0505}{x_M^{1/6}}\left(1+\frac{0.40}{x_M^{1/4}}+\frac{0.5316}{x_M^{1/2}}\right)\exp(-1.8899x_M^{1/3}). \quad \text{(B25)}$$

Integrating Eq. B23 we find the total emissivity

$$\epsilon^{\rm (sy)} = 3.61\times10^{-34}n_{\rm e}B^2T_{\rm e}^2, \quad \text{(B26)}$$

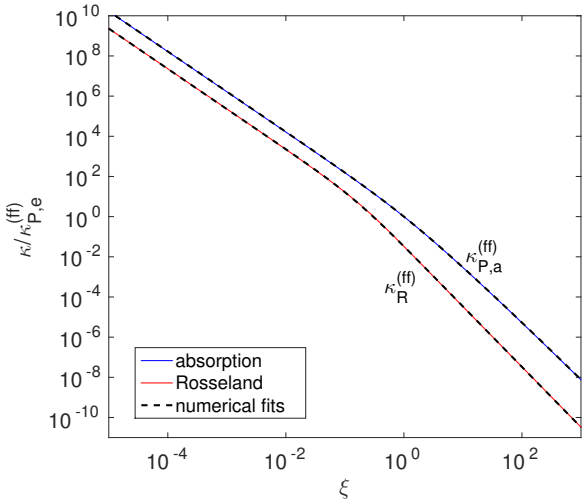

Figure B1. Opacities used for the bremsstrahlung radiation. Error of fits for the shown range of parameter ξ is less than 5%.

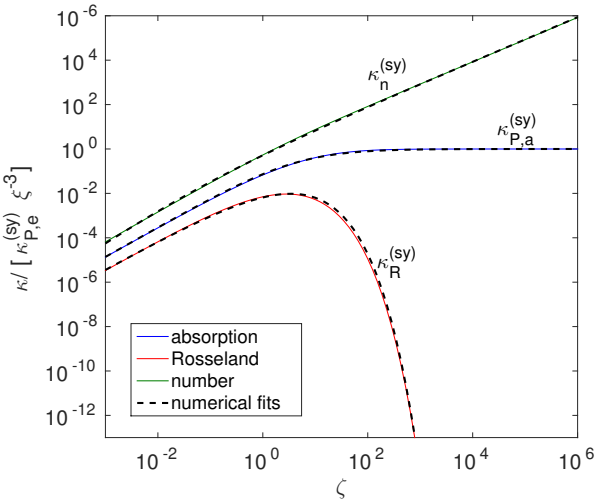

Figure B2. Opacities used for the synchrotron radiation. Error of fits for the shown range of parameter ζ is less than 15% for $\kappa_{\rm n}^{(\rm sy)}$ and $\kappa_{\rm P,a}^{(\rm sy)}$. The fitting error is slightly larger in case of $\kappa_{\rm R}^{(\rm sy)}$, because of the high variability of this distribution. However, this mostly affects the region of large ζ, where Rosseland opacity becomes negligible anyway.

which allows to find the emission energy mean opacity

$$\kappa_{\rm P,e}^{(\rm sy)}\rho = \frac{\epsilon^{(\rm sy)}}{4\sigma T_{\rm e}^4} = 1.59\times10^{-30} n_{\rm e} B^2 T_{\rm e}^{-2}\ [\rm cm^{-1}]. \tag{B27}$$

We proceed by employing the Rayleigh-Jeans approximation, since synchrotron processes are generally at very low frequencies ($h\nu \ll kT_{\rm e}$). We then obtain the frequency resolved opacity function κ_ν with the use of the Eq. B1,

$$\kappa_\nu^{(\rm sy)}\rho = 2.13\times10^{39} n_{\rm e} B^{-1} T_{\rm e}^{-5}\,\frac{I'(x_M)}{x_M}[\rm cm^{-1}Hz^{-1}]. \tag{B28}$$

We define a dimensionless parameter ζ

$$\zeta = \frac{kT_{\rm r}}{h\nu_M} = 1.745\times10^{23}\xi\left[\frac{B}{1G}\frac{T_{\rm e}}{1K}\right]^{-1}, \tag{B29}$$

where $\xi = T_{\rm r}/T_{\rm e}$, so that $h\nu/kT_{\rm r} = x_M/\zeta$. Remaining mean opacities can be found by evaluating integrals B3, B5 and B8,

$$\begin{aligned}
\kappa_{\rm R}^{(\rm sy)}\rho &= 4.01\times10^{-31} n_{\rm e} B^2 T_{\rm e}^{-2}\xi^{-3}\zeta^8\frac{I_4}{I_6(\zeta)}\\
&= \kappa_{\rm P,e}^{(\rm sy)}\rho\,\xi^{-3} 6.54\,\zeta^8 I_6^{-1}(\zeta)\\
&\approx \kappa_{\rm P,e}^{(\rm sy)}\rho\,\xi^{-3}\cdot 3.24\times10^{-2}\zeta^{1.31}\exp\left(-1.60\zeta^{0.463}\right),
\end{aligned} \tag{B30}$$

$$\begin{aligned}
\kappa_{\rm P,a}^{(\rm sy)}\rho &= 4.01\times10^{-31} n_{\rm e} B^2 T_{\rm e}^{-2}\xi^{-3}\zeta^{-1}\frac{I_7(\zeta)}{I_2}\\
&= \kappa_{\rm P,e}^{(\rm sy)}\rho\,\xi^{-3} 3.88\times10^{-2}\zeta^{-1} I_7(\zeta)\\
&\approx \kappa_{\rm P,e}^{(\rm sy)}\rho\,\xi^{-3}\left(1+5.444\zeta^{-2/3}+7.218\zeta^{-4/3}\right)^{-1},
\end{aligned} \tag{B31}$$

$$\begin{aligned}
\kappa_{\rm n}^{(\rm sy)}\rho &= 4.01\times10^{-31} n_{\rm e} B^2 T_{\rm e}^{-2}\xi^{-3}\frac{I_8(\zeta)}{I_9}\\
&= \kappa_{\rm P,e}^{(\rm sy)}\rho\,\xi^{-3} 1.05\times10^{-1} I_8(\zeta)\\
&\approx \kappa_{\rm P,e}^{(\rm sy)}\rho\,\xi^{-3}\cdot 0.868\zeta\left(1+0.589\zeta^{-1/3}+0.087\zeta^{-2/3}\right)^{-1}.
\end{aligned} \tag{B32}$$

where the relevant integrals are

$$\begin{aligned}
I_6(\zeta) &= \int_0^\infty \frac{x_M^5\exp(x_M/\zeta)dx_M}{I'(x_M)[\exp(x_M/\zeta)-1]^2}\\
&\approx 202\zeta^{6.69}\exp\left(1.60\zeta^{0.463}\right),
\end{aligned} \tag{B33}$$

$$\begin{aligned}
I_7(\zeta) &= \int_0^\infty \frac{I'(x_M)x_M^2 dx_M}{[\exp(x_M/\zeta)-1]}\\
&\approx \frac{26.0\zeta}{1+5.444\zeta^{-2/3}+7.218\zeta^{-4/3}},
\end{aligned} \tag{B34}$$

$$\begin{aligned}
I_8(\zeta) &= \int_0^\infty \frac{I'(x_M)x_M dx_M}{[\exp(x_M/\zeta)-1]}\\
&\approx \frac{8.27\zeta}{1+0.589\zeta^{-1/3}+0.087\zeta^{-2/3}},
\end{aligned} \tag{B35}$$

$$I_9 = \int_0^\infty \frac{x^2 dx}{\exp(x)-1} \approx 2.404. \tag{B36}$$

The accuracy of the fitting formulas given by Eqs. B30 - B32 is indicated in Fig. B2. Finally, we evaluate the rate at which photons are produced by the synchrotron process by direct integration,

$$\widehat{n}_{\rm sy} = \int_0^\infty \frac{\epsilon_\nu^{(\rm sy)}}{h\nu}d\nu = 1.44\times10^5 B n_{\rm e}\ [\rm cm^{-3}s^{-1}]. \tag{B37}$$